

High-resolution numerical relaxation approximations to second-order macroscopic traffic flow models

A. I. Delis^{a,*}, I. K. Nikolos^a, M. Papageorgiou^a

^a*School of Production Engineering & Management, Technical University of Crete, Chania, Greece*

Abstract

A novel numerical approach for the approximation of several, widely applied, macroscopic traffic flow models is presented. A relaxation-type approximation of second-order non-equilibrium models, written in conservation or balance law form, is considered. Using the relaxation approximation, the nonlinear equations are transformed to a semi-linear diagonalizable problem with linear characteristic variables and stiff source terms. To discretize the resulting relaxation system, low- and high-resolution reconstructions in space and implicit-explicit Runge-Kutta time integration schemes are considered. The family of spatial discretizations includes a second-order MUSCL scheme and a fifth-order WENO scheme, and a detailed formulation of the scheme is presented. Emphasis is given on the WENO scheme and its performance for solving the different traffic models. To demonstrate the effectiveness of the proposed approach, extensive numerical tests are performed for the different models. The computations reported here demonstrate the simplicity and versatility of relaxation schemes as solvers for macroscopic traffic flow models.

Keywords: Second-order traffic flow models; Numerical modeling; Relaxation schemes; High-resolution

1. Introduction

Traffic flow modeling has attracted a rapidly growing interest over the past years, due to the need for optimization of the usage of existing traffic infrastructure and the design of new structures, the growing economic/environmental cost of traffic jams, their impact on the quality of life, the need to assess and optimize new driver assistance devices, and (from a scientific point of view) the existence of complicated non-linear dynamical phenomena associated with traffic flow and the characteristics of vehicles and drivers' behavior. The effective modeling of such phenomena, like traffic jams, stop-and-go traffic and "synchronized" congested traffic [27], call for the development of accurate theoretical models which should reproduce, at least qualitatively, all traffic states with the minimum number of parameters [25] and the corresponding computational procedures,

*Corresponding author. Tel.: +302821037751

Email address: adelis@science.tuc.gr (A. I. Delis)

which should be numerically efficient (in terms of computational time and memory requirements), accurate and robust, to allow for their use in real-world simulation and optimization scenarios.

Several approaches have been followed over the past years to model the dynamics of traffic flow, the most successful being cellular automata, microscopic car-following models, gas-kinetic models, and macroscopic traffic models. Comprehensive descriptions of such models can be found, for example, in [25, 31, 7, 56]. Macroscopic models consider the traffic as an anisotropic fluid (continuum), where vehicle dynamics are described in terms of spatial vehicle density and average velocity, as functions of location and time. Some of the advantages of the macroscopic models are (a) their numerical efficiency (compared to microscopic ones), (b) their good agreement with empirical data, (c) their suitability for analytical investigations, (d) the simple treatment of inflows, and (e) the possibility to simulate multi-lane flows by effective one-lane models, we refer, for example, to [25] and [27] for thorough discussions.

The main motivation behind this work is the development of a common numerical framework for the macroscopic simulation of traffic flow networks, transparent to the traffic flow model used (only second-order non-equilibrium traffic flow models are considered in this work). New models, especially for Adaptive Cruise Control (ACC) and Cooperative Adaptive Cruise Control (CACC) simulations, may be straightforwardly introduced in this framework and thus, compared and tested under common conditions. The requirement for the use of different macroscopic models (existing or new developments) under the same environment, imposes the avoidance of developing new complex numerical solvers. For example, the adoption of a numerical approach based on Godunov-type schemes with (exact or approximate) Riemann solvers would require the development of new different solver for each new model introduced to the framework, as for example in [10, 23, 57]. The second objective is to explore and exploit the advantages of high-order numerical schemes for space and time discretization, in terms of computational efficiency and accuracy, to evaluate such schemes and to compare them to lower-order ones for different second-order traffic flow models.

The approach that is followed here includes the adoption of the relaxation approach proposed in [34] and is based on Finite Volume numerical discretizations of a linearized system of differential equations, which renders the methodology independent of the use of Riemann solvers (approximate or not). Within this approach, the differences between the various traffic flow models are taken into account through the corresponding flux and source term functions, plus their different parameters and upper bounds of the corresponding eigenvalues of the flux's Jacobian. Different spatial discretization schemes are incorporated in a common computational framework; a first-order upwind scheme, a second-order Monotone Upstream-centered Scheme for Conservation Laws (MUSCL) and a fifth-order weighted essentially non-oscillatory (WENO) scheme are introduced and thoroughly tested. Higher-order implicit-explicit (IMEX) Runge-Kutta (RK) schemes are also introduced for time discretization. The computational framework is formulated as to have a generalized description of variables and fluxes and to deal with different traffic flow models and future modifications.

Although low-order finite volume schemes have been successfully applied to macroscopic traffic flow modeling (we refer, for example, to [24, 44, 8, 45]), high-order schemes are able of reducing the numerical dissipation and producing sharper resolution in the numerical solutions. As a

result, fewer discretization points are needed for a desired accuracy and the computation becomes much more efficient, compared to first-order discretization schemes. Moreover, as it will be demonstrated in following sections, specific features of the solution for some problems can be obtained only if high-order schemes are implemented. Important traffic flow conditions, such as shock waves corresponding, for instance, to queue tails, stop-and-go phenomena and cluster formations, should be accurately reproduced by a numerical scheme.

WENO schemes have been applied, mainly, to the Lighthill-Whitham-Richards (LWR), [39, 49], first-order macroscopic flow model and its variants, and by very few research groups so far. The fifth-order Finite Difference WENO scheme of [32], with Lax-Friedrichs flux splitting for each equation in the system, was applied in [62] to solve the multi-class extension, proposed in [59], of the LWR model (MCLWR) with heterogeneous drivers. An extension to this work was presented in [64] to approximate an MCLWR model, modified to deal with inhomogeneous road conditions; a fifth-order accurate component-wise WENO scheme was used, which applies the Lax-Friedrichs numerical flux in the Finite Volume method and the flux splitting in the Finite Difference method. An extension of the work from [62] was presented in [65], where better estimation of the minimal characteristic speed of the MCLWR model was provided, thus improving the numerical results. In [9] a family of numerical schemes was proposed for multi-species kinematic flows with discontinuous fluxes, including an MCLWR traffic flow model. These first-order schemes can be upgraded to higher-order accuracy by employing MUSCL-type techniques.

The relaxation approach introduced in [34], has found wide application in fluid dynamics problems, we refer for example to [4, 6, 13, 18, 20, 19, 21, 22, 36, 50, 51, 52, 5], among others. The main advantage of such schemes is that neither Riemann solvers, nor the computation of eigenvalues are needed, which renders this methodology ideal for problems where an analytic expression for the eigenvalues of the systems' Jacobian matrix may not be possible or is computationally tedious to obtain, or the Riemann problems are difficult to approximate [53]. However, the work on relaxation schemes for traffic flow problems includes, thus far, very few works on second- or higher-order schemes on the LWR (and variants) and low-order schemes on standard second-order traffic flow models such as the Aw and Rascle (AR)[2] and the Aw-Rascle-Zhang (ARZ) models [60].

In [53] a multi-lane LWR model was used as a test model for evaluating a relaxation scheme, developed in Eulerian and Lagrangian (characteristic) frameworks, using IMEX Runge-Kutta (RK) schemes for time integration. In the Eulerian framework a second-order MUSCL scheme was developed, and compared to the characteristic scheme and to a simple upwind one, providing in general the sharpest results. In [30] relaxation schemes, utilizing a second-order central WENO scheme for spatial discretization and a third-order IMEX RK method, were used to approximate simple discrete-velocity models of traffic flows, which reduce to the LWR model in the small relaxation limit. A relaxation scheme for the MCLWR model with heterogeneous drivers was presented in [14]. As an extension to this work, a high-resolution relaxed scheme, based on a fifth-order WENO reconstruction was presented in [15] for the MCLWR model on an inhomogeneous highway, combined with a third-order strong stability preserving (SSP) RK method for time discretization. In [1] a relaxation scheme was used, combined with a first-order upwind scheme,

and a second-order MUSCL scheme for spatial discretization along with a second-order IMEX RK scheme for temporal discretization. The schemes are used for the simulation of first-order (LWR) and second-order (AR, ARZ) traffic flow models in various Riemann problems, where the superiority of the MUSCL scheme over the first-order one was demonstrated.

The contribution of the present work includes the following: (a) utilization of a relaxation scheme for the numerical solution of different second-order traffic flow models; (b) utilization of high-order spatial and temporal numerical discretization schemes; (c) generalized formulation of the numerical procedure transparent to the traffic flow model - different second-order traffic flow models can be simulated under the same framework; (d) testing of the procedure for a large number of representative test cases and evaluation of the advantages of the high-order numerical discretizations relative to low-order ones (in terms of accuracy and computational efficiency). The rest of the paper is organized as follows: In Section 2 the second-order macroscopic traffic flow models used in this work are presented. In Section 3 the adopted relaxation model for the 1-D systems of conservation laws is described in detail. Section 4 contains the details of numerical discretization in space and time; the first-order upwind scheme, the second-order MUSCL scheme and the fifth-order WENO scheme used are presented, along with the high-order IMEX RK methods for time discretization. Details on the implementation of the initial and boundary conditions are also discussed. Section 5 contains an extensive numerical evaluation and comparison of the proposed schemes for all the considered traffic flow models in representative test cases. The work is concluded in Section 6.

2. Macroscopic traffic flow models

We consider the numerical approximation of macroscopic non-equilibrium two-equation traffic flow models, with a possible source term present, all written in as nonlinear systems of conservation laws in one space dimension, with initial data, as

$$\begin{aligned}\partial_t \mathbf{u} + \partial_x \mathbf{f}(\mathbf{u}) &= \mathbf{s}(\mathbf{u}), \\ \mathbf{u}(x, 0) &= \mathbf{u}_0(x),\end{aligned}\tag{1}$$

where the functions \mathbf{u} , $\mathbf{f}(\mathbf{u})$ and $\mathbf{s}(\mathbf{u}) \in \mathbb{R}^2$. When the source term $\mathbf{s}(\mathbf{u})$ is present system, (1) is called a balance law. In what follows, we will denote, as functions in space x and time t , $\rho(x, t)$ the car or traffic density (number of cars per unit area), $u(x, t)$ the average speed and $f(\rho, u) \equiv q = \rho u$ the traffic flow rate.

Systems in the form of (1) can be rewritten in quasi-linear form

$$\partial_t \mathbf{u} + \mathbf{J}(\mathbf{u}) \partial_x \mathbf{u} = \mathbf{s}(\mathbf{u}),\tag{2}$$

where $\mathbf{J}(\mathbf{u}) = \frac{\partial \mathbf{f}}{\partial \mathbf{u}}$ is the Jacobian matrix of the system. Solving for the eigenvalues (characteristic speeds) from $\det[\mathbf{J}(\mathbf{u}) - \lambda \mathbf{I}] = 0$, certain realistic characteristics of the traffic models can be verified

or not, e.g. the anisotropic nature of traffic flow. Real and distinct eigenvalues $\lambda_{1,2}$ guarantee hyperbolicity (and linearly independent right eigenvectors). The solutions related to the k -th eigenvalue are called k -family wave solutions.

Of particular interest, also in this work, is the case where the initial data is given as a Riemann problem. That is, with the following piecewise constant initial data having a single discontinuity around location \bar{x} ,

$$\mathbf{u}_0(x) = \begin{cases} \mathbf{u}_l & \text{for } x < \bar{x}, \\ \mathbf{u}_r & \text{for } x > \bar{x}. \end{cases} \quad (3)$$

Depending on the model equations and by the relationship between left, \mathbf{u}_l , and right, \mathbf{u}_r , states, different k -families of elementary wave solutions exist. These elementary wave solutions are constituted by shock waves, rarefaction waves and contact discontinuities. The correct numerical representation of these elementary solutions is a requirement by any numerical scheme approximating (1).

2.1. The PW model

The Payne-Whitham (PW) model, proposed independently in [47] and [58], is one of the first non-equilibrium traffic models and is given in conservation law form as

$$\begin{cases} \partial_t \rho + \partial_x(\rho u) = 0; \\ \partial_t(\rho u) + \partial_x(\rho u^2 + P(\rho)) = \rho \left(\frac{V^e(\rho) - u}{\tau} \right) \end{cases} \quad (4)$$

where $P(\rho) = C_0^2 \rho$ is the pressure-like term of the flow, with C_0 being the anticipation parameter that describes the macroscopic response of the driver to the traffic density. The model also includes a traffic relaxation term that keeps speed concentration in equilibrium, with $V^e(\rho)$ being the equilibrium speed (maximum out-of danger velocity meant to mimic driver's behavior) and τ being a relaxation time. In addition, with $f^e(\rho, V^e) = \rho V^e(\rho)$ we can denote the so-called fundamental diagram.

For this model the general form of the balance law (1) is satisfied for $\mathbf{u} = [\rho, \rho u]^T$, $\mathbf{f}(\mathbf{u}) = [\rho u, \rho u^2 + P(\rho)]^T$ and $\mathbf{s}(\mathbf{u}) = [0, (\rho V^e(\rho) - \rho u)/\tau]^T$. Solving for the eigenvalues, we get two distinct and real ones

$$\lambda_{1,2} = u \pm C_0.$$

These second-order wave speeds are usually called frozen "characteristic speeds". Further, the PW model has a sub-characteristic wave speed (relative to the road), $\lambda_\star = V^e(\rho) + \rho V^{e'}(\rho)$, which is actually the wave speed of the LWR model. It should be noted that, as $\tau \rightarrow 0$, system (4) admits as its limit the viscous LWR model. The PW model can be considered as a system of hyperbolic conservation laws with relaxation in the sense of Whitham [58] and Liu [40]. In [58] it was shown that the stability condition for the linearized system with relaxation is

$$\lambda_1 < \lambda_\star < \lambda_2$$

This model has a major drawback that researchers (see for example [17] and [16]) have been concerned about, mainly, that this model strongly follows the fluid flow theory. The anisotropic nature of traffic is not preserved, since the vehicles are allowed to move with negative speed i.e. against the flow. This is clear from the eigenvalues, where one is always greater than the vehicle speed u . Thus, information from behind affects the behavior of the driver. This is not necessarily a physical contradiction since u is an average of vehicle and freeway-lane speeds [46, 63], see also [28]. Therefore, we consider this model here since and are interested in its numerical solution and its behavior to the proposed numerical schemed presented later on. For $P(\rho)$, various expressions have been propose, we refer to [41] for an overview. Here we use the model parameters given in [33, 29, 35, 61], i.e., $V^e(\rho) = 5.0461 \left[(1 + \exp((\rho - 0.25)/0.06))^{-1} - 3.72 \cdot 10^{-6} \right] \tilde{l}/\tilde{\tau}$, with \tilde{l} and $\tilde{\tau}$ being the unit of length and time, respectively, and $C_0 = 2.48445\tilde{l}/\tilde{\tau}$.

2.2. The Aw-Rascle (AR) and the Aw-Rascle-Zang (ARZ) models

Aw and Rascle [2] proposed a new two-equation traffic flow model that improved the PW and related models and addressed the concerns raised by moving away of fluids and toward the anisotropic property of the traffic. They suggested that the correct dependence must involve the total derivative of the pressure-like terms. Thus, the AR model in conservation law form reads as

$$\begin{cases} \partial_t \rho + \partial_x(\rho u) = 0; \\ \partial_t(\rho(u + P(\rho))) + \partial_x(\rho u(u + P(\rho))) = 0, \end{cases} \quad (5)$$

where now $P(\rho)$ is an increasing function of density, so as to insure that the model carries the anisotropic property, given as

$$P(\rho) = C_0^2 \rho^\gamma, \quad \gamma > 0.$$

Indeed, solving for the eigenvalues two distinct and real ones can be found

$$\lambda_1 = u - \rho P'(\rho) \quad \text{and} \quad \lambda_2 = u,$$

except for $\rho = 0$, i.e. at vacuum. The system is strictly hyperbolic, except for $\rho = 0$, and since the "pressure" is an increasing function, it is guaranteed that $\lambda_1 < \lambda_2$. In this work, we use the values $C_0 = 1$ and $\gamma = 2$.

A model similar to the AR model above was proposed in [60] but with its second equation derived from a *microscopic car-following model*. Hence, a micro-to-macro link is established for this model. The basic ARZ model, in its conservative form, is given as

$$\begin{cases} \partial_t \rho + \partial_x(\chi + \rho V^e(\rho)) = 0; \\ \partial_t \chi + \partial_x \left(\frac{\chi^2}{\rho} - \chi V^e(\rho) \right) = 0, \quad \chi = \rho(u - V^e(\rho)), \end{cases}$$

where $V^e(\rho)$ is the equilibrium velocity and variable χ can be considered to be the difference between the actual flow ($q = \rho u$) and equilibrium flow ($q^e = \rho V^e$). In this work, for the sake of

brevity, only Greenshield's model for the equilibrium velocity is implemented, given as,

$$V^e(\rho) = u_{\max} \left(1 - \frac{\rho}{\rho_{\max}} \right)$$

where u_{\max} is the free flow speed and ρ_{\max} is the maximum (jam) density.

Finally, by solving for the eigenvalues we find two distinct and real eigenvalues

$$\lambda_1 = u + \rho(V^e)' \quad \text{and} \quad \lambda_2 = u$$

therefore this system is again strictly hyperbolic and since $(V^e)'$ is negative, the maximum the information can travel is equal to the vehicle speed u .

We point out here that, both the AR and ARZ models are strictly hyperbolic except for $\rho = 0$ i.e., at vacuums, where their two eigenvalues are equal. This case may constitute a particular challenge for a numerical scheme, which should correctly resolve this case.

2.3. The non-local Gas-Kinetic based traffic model

In [55] (see also [26] and [56]) a macroscopic gas-kinetic-based traffic flow model (GKT model) was proposed, derived from microscopic vehicle dynamics.

In conservation law (balance law) form this model is written as

$$\begin{cases} \partial_t \rho + \partial_x(\rho u) = 0, \\ \partial_t(\rho u) + \partial_x(\rho u^2 + \Theta \rho) = \rho \left(\frac{V^e(\rho) - u}{\tau} \right), \end{cases} \quad (6)$$

where $\Theta = A(\rho)u^2$, with $A(\rho)$ being a density dependent variance factor, given as:

$$A(\rho) = A_0 + \delta A \left[1 + \tanh \left(\frac{\rho - \rho_{cr}}{\delta \rho} \right) \right]$$

in which ρ_{cr} is the critical density, reflecting the division between the free flow and congested traffic situation. The constants A_0 , δA and $\delta \rho$ are given in Table 1, along with other typical values for this model following [55, 26]. $V^e(\rho, u, \rho_a, u_a)$ denotes again the (non-local and dynamic) equilibrium speed, which now depends not only on the local density ρ and mean speed u but also on the non-local density ρ_a and mean speed u_a , and is defined as

$$V^e(\rho, u, \rho_a, u_a) = v_{\max} \left[1 - \frac{A(\rho)}{2A(\rho_{\max})} \left(\frac{\rho_a T u}{1 - \rho_a / \rho_{\max}} \right)^2 B(\delta u) \right]. \quad (7)$$

According to (7), V^e is given by the maximum (desired) velocity u_{\max} , reduced by a term that reflects necessary deceleration maneuvers. Both ρ_a and u_a are computed at location $x_a = x + \gamma(1/\rho_{\max} + T \cdot u)$ with T being the safe time headway and γ a scale parameter with $\gamma \in [1, 2]$. Finally,

B is a so-called Boltzmann (interaction) factor, and with $\delta u = \frac{u - u_a}{\sqrt{2\Theta}}$ this factor is determined as

$$B(z) = 2 \left[z \frac{e^{-z^2/2}}{\sqrt{2\pi}} + (1 + z^2) \int_{-\infty}^z \frac{e^{-y^2/2}}{\sqrt{2\pi}} dy \right]$$

and describes the dependence of the braking interaction on the dimensionless velocity difference δu between the actual location x and interaction location x_a .

The main difference between the GKT model and other macroscopic traffic models is its non-local character. The non-local term in (7) has smoothing properties similar to those of a viscosity term, but its effect is forwardly directed and, therefore, more realistic. The Jacobian of the model (6) has two distinct eigenvalues $\lambda_{1,2} = u \pm C$ where $C = \sqrt{\partial\Theta/\partial\rho}$ which indicate that the model is also strictly hyperbolic.

Parameters	Units	Value
Free speed, u_{\max}	km/h	110
Jam density, ρ_{\max}	vehicle/km	160
Critical density, ρ_{cr}	vehicle /km	$0.27\rho_{\max}$
Time headway, T	s	1.8
Scaled factor, γ		1.2
Relaxation time, τ	s	3.2
A_0		0.008
δA		$2.5A_0$
$\delta\rho$	vehicle /km	$0.05 \rho_{\max}$

Table 1: Typical model parameters used for the GKT traffic model (6)

3. The relaxation model for 1-D systems of conservation laws

In this section we briefly present the class of relaxation models introduced in [34]. Consider an extended (with a general source term present) nonlinear system of conservation laws in one space dimension (1D), with initial data,

$$\begin{aligned} \partial_t \mathbf{u} + \partial_x \mathbf{f}(\mathbf{u}) &= \mathbf{s}(\mathbf{u}), \\ \mathbf{u}(x, 0) &= \mathbf{u}_0(x), \end{aligned} \tag{8}$$

where the functions \mathbf{u} and $\mathbf{f}(\mathbf{u}) \in \mathbb{R}^n$. Introducing the artificial variable \mathbf{v} (relaxation variable), the corresponding relaxation system is then given by

$$\begin{aligned}\partial_t \mathbf{u} + \partial_x \mathbf{v} &= \mathbf{s}(\mathbf{u}), \\ \partial_t \mathbf{v} + \mathbf{C}^2 \partial_x \mathbf{u} &= -\frac{1}{\epsilon} (\mathbf{v} - \mathbf{f}(\mathbf{u})),\end{aligned}\tag{9}$$

with initial data

$$\begin{aligned}\mathbf{u}(x, 0) &= \mathbf{u}_0(x), \\ \mathbf{v}(x, 0) &= \mathbf{v}_0(x) = \mathbf{f}(\mathbf{u}_0(x)),\end{aligned}$$

where the small parameter ϵ is the *relaxation rate* ($0 < \epsilon \ll 1$) and

$$\mathbf{C}^2 = \text{diag}\{c_1^2, c_2^2, \dots, c_n^2\}$$

is a positive diagonal matrix to be chosen.

For small ϵ , applying the Chapman-Enskog expansion in the relaxation system (9), see for example [11, 12, 34], we can derive the following approximation for \mathbf{u}

$$\partial_t \mathbf{u} + \partial_x \mathbf{f}(\mathbf{u}) = \mathbf{s}(\mathbf{u}) + \epsilon \partial_x [\mathbf{f}'(\mathbf{u}) \mathbf{s}(\mathbf{u})] + \epsilon \partial_x \left[(\mathbf{C}^2 - \mathbf{f}'(\mathbf{u})^2) \partial_x \mathbf{u} \right] + O(\epsilon^2),\tag{10}$$

where $\mathbf{f}'(\mathbf{u})$ symbolizes the Jacobian matrix of the flux \mathbf{f} . Equation (10) governs the first-order behavior of the relaxation system (9), with the third term on the right-hand side being an $O(\epsilon)$ dominant dissipation term in the model and $(\mathbf{C}^2 - \mathbf{f}'(\mathbf{u})^2)$ being the diffusion coefficient matrix. Model (9) is well-posed only if $(\mathbf{C}^2 - \mathbf{f}'(\mathbf{u})^2)$ is positive semi-definite for all \mathbf{u} . This requirement on the diffusion coefficient matrix is the well-known *sub-characteristic condition*, [34], i.e.

$$\mathbf{C}^2 - \mathbf{f}'(\mathbf{u})^2 \geq 0, \quad \forall \mathbf{u},\tag{11}$$

which ensures the dissipative nature of (10). In 1D, it is equivalent to

$$\lambda^2 \leq c^2, \quad \text{where } \lambda = \max_{1 \leq i \leq n} |\lambda_i| \quad \text{and} \quad c = \min_{1 \leq i \leq n} |c_i|.\tag{12}$$

It is clear that for \mathbf{u} varying in a bounded domain, equation (11) can always be satisfied by choosing sufficiently large values for the diagonal elements in \mathbf{C}^2 . However, because of the stability constraints on a numerical scheme, it is desirable to obtain the smallest values for \mathbf{C}^2 meeting the criterion (11). Details of the choice of \mathbf{C}^2 are given in Section 4.4.

The, now, linear system (9) can be further written as:

$$\begin{bmatrix} \partial_t \mathbf{u} \\ \partial_t \mathbf{v} \end{bmatrix} + \begin{bmatrix} 0 & \mathbf{I} \\ \mathbf{C}^2 & 0 \end{bmatrix} \begin{bmatrix} \partial_x \mathbf{u} \\ \partial_x \mathbf{v} \end{bmatrix} = \begin{bmatrix} \mathbf{s}(\mathbf{u}) \\ -\frac{1}{\epsilon} (\mathbf{v} - \mathbf{f}(\mathbf{u})) \end{bmatrix}.\tag{13}$$

By eliminating \mathbf{v} from (13) we can obtain the following regularization of the original system

$$\partial_t \mathbf{u} + \partial_x \mathbf{f}(\mathbf{u}) = \mathbf{s}(\mathbf{u}) + \epsilon \partial_t \mathbf{s}(\mathbf{u}) - \epsilon (\partial_t^2 \mathbf{u} - \mathbf{C}^2 \partial_{xx}^2 \mathbf{u}), \quad (14)$$

that introduces a higher order wave type regularization of the original conservation law and the additional term $\epsilon \partial_t \mathbf{s}(\mathbf{u})$.

The rigorous theory of relaxation approximation for solutions with shocks is well developed when the limit equation is scalar. In [11, 12, 43] it was shown that solutions of the relaxation model (9) converge strongly to the unique entropy solution of the original conservation laws. The relaxation model provides a subtle dissipative mechanism against the destabilizing effect of nonlinear response, as well as a damping mechanism on oscillations.

4. Numerical Discretizations

Assuming for the moment that $\mathbf{s}(\mathbf{u}) = 0$, and considering the relaxation system (13) this can be further re-written as

$$\partial_t \mathbf{W} + \mathbf{M} \partial_x \mathbf{W} = \mathbf{H} \quad (15)$$

where

$$\mathbf{W} = \begin{bmatrix} \mathbf{u} \\ \mathbf{v} \end{bmatrix}, \quad \mathbf{M} = \begin{bmatrix} 0 & \mathbf{I} \\ \mathbf{C}^2 & 0 \end{bmatrix} \quad \text{and} \quad \mathbf{H} = \begin{bmatrix} 0 \\ -\frac{1}{\epsilon}(\mathbf{v} - \mathbf{f}(\mathbf{u})) \end{bmatrix}. \quad (16)$$

Since system (15) is hyperbolic, matrix \mathbf{M} can be diagonalized as

$$\mathbf{M} = \mathbf{S} \mathbf{\Lambda} \mathbf{S}^{-1} \quad \text{or} \quad \mathbf{\Lambda} = \mathbf{S}^{-1} \mathbf{M} \mathbf{S}$$

where \mathbf{S} is the matrix of the right eigenvectors of \mathbf{M} , and $\mathbf{\Lambda}$ is the diagonal matrix with the diagonal elements being the eigenvalues of \mathbf{M} . By introducing characteristic variables, the relaxation system can be de-coupled. By defining the characteristic variables as

$$\mathbf{G} = \mathbf{S}^{-1} \mathbf{W}$$

the following de-coupled diagonal system is obtained

$$\partial_t \mathbf{G} + \mathbf{\Lambda} \partial_x \mathbf{G} = \mathbf{S}^{-1} \mathbf{H}. \quad (17)$$

After some simple algebraic manipulations, system (17) can be written as

$$\begin{bmatrix} \partial_t(\mathbf{C}\mathbf{u} + \mathbf{v}) \\ \partial_t(\mathbf{C}\mathbf{u} - \mathbf{v}) \end{bmatrix} + \mathbf{\Lambda} \begin{bmatrix} \partial_x(\mathbf{C}\mathbf{u} + \mathbf{v}) \\ \partial_x(\mathbf{C}\mathbf{u} - \mathbf{v}) \end{bmatrix} = \begin{bmatrix} -\frac{1}{\epsilon}(\mathbf{v} - \mathbf{f}(\mathbf{u})) \\ \frac{1}{\epsilon}(\mathbf{v} - \mathbf{f}(\mathbf{u})) \end{bmatrix}, \quad (18)$$

with $\mathbf{\Lambda} = \text{diag}\{(c_1, c_2, \dots, c_n, -c_1, -c_2, \dots, -c_n)\}$. Thus, the left-hand side of the above decoupled hyperbolic equations is linear with constant wave speeds neatly split into positive and negative

parts. So, the solution of (17) has the property that it propagates at finite speeds along linear characteristic curves. Systems (17) and (15) are equivalent such that a discretization of each one of them leads essentially to the discretization of the other. From (18) and by setting $\mathbf{g}_{1,2} = \mathbf{v} \pm \mathbf{C}\mathbf{u}$, the following expressions can be obtained for \mathbf{u} and \mathbf{v} :

$$\mathbf{u} = \frac{1}{2}\mathbf{C}^{-1}(\mathbf{g}_1 - \mathbf{g}_2) \quad \text{and} \quad \mathbf{v} = \frac{1}{2}(\mathbf{g}_1 + \mathbf{g}_2), \quad (19)$$

thus, the original variables of the relaxation system, \mathbf{u} and \mathbf{v} , can be recovered. As noted in the previous sections, the main advantage of numerically solving the relaxation system over the original conservation law lies in this special structure of the linear characteristic fields. Constructing an upwind scheme for the above system is much simpler compared to the task of developing an upwind scheme for the original nonlinear conservation laws.

To discretize the system, let $x_i = i\Delta x$, $x_{i\pm\frac{1}{2}} = (i\pm\frac{1}{2})\Delta x$, where, for simplicity, we assume that Δx is a uniform spatial step. The approximate cell average of the variable \mathbf{u} in the cell $I_i = [x_{i-\frac{1}{2}}, x_{i+\frac{1}{2}}]$ at time t is denoted as $\mathbf{u}_i(t)$, i.e.,

$$\mathbf{u}_i(t) = \frac{1}{\Delta x} \int_{I_i} \mathbf{u}(x, t) dx,$$

and the approximate value of \mathbf{u} at $(x_{i+\frac{1}{2}}, t)$ by $\mathbf{u}_{i+\frac{1}{2}}(t)$. Integrating (9) and keeping the time continuous, the semi-discrete relaxation system is given as

$$\begin{aligned} \frac{\partial}{\partial t} \mathbf{u}_i + \frac{1}{\Delta x} (\mathbf{v}_{i+\frac{1}{2}} - \mathbf{v}_{i-\frac{1}{2}}) &= \mathbf{s}(\mathbf{u})_i, \\ \frac{\partial}{\partial t} \mathbf{v}_i + \frac{\mathbf{C}^2}{\Delta x} (\mathbf{u}_{i+\frac{1}{2}} - \mathbf{u}_{i-\frac{1}{2}}) &= -\frac{1}{\epsilon} (\mathbf{v}_i - \mathbf{f}(\mathbf{u})_i). \end{aligned} \quad (20)$$

where $\mathbf{s}(\mathbf{u})_i$ and $\mathbf{f}(\mathbf{u})_i$ are space averages of the source term and flux function, respectively. To complete the spatial discretization, it is necessary to evaluate the flux values $\mathbf{u}_{i\pm\frac{1}{2}}$ and $\mathbf{v}_{i\pm\frac{1}{2}}$.

Remark 1. One can further consider the so-called relaxed system, [34], resulting from system (20) in the limit $\epsilon \rightarrow 0$, which is given by

$$\begin{aligned} \frac{\partial}{\partial t} \mathbf{u}_i + \frac{1}{\Delta x} (\mathbf{v}_{i+\frac{1}{2}} - \mathbf{v}_{i-\frac{1}{2}}) &= \mathbf{s}(\mathbf{u})_i, \\ \mathbf{v}_i &= \mathbf{f}(\mathbf{u})_i. \end{aligned} \quad (21)$$

System (21) is independent of the small relaxation rate and the artificial relaxation variables. However, we do not consider this approach in this presentation since it will be reported in future work.

Since system (9) has linear characteristics, with constant characteristic speeds, $+c_k$ and $-c_k$, upwind schemes can be implemented relatively straightforwardly. For example, the *first-order upwind* scheme, [34, 18], applied to \mathbf{g}_1 and \mathbf{g}_2 gives

$$\mathbf{g}_{1_{i+\frac{1}{2}}} = \mathbf{g}_{1_i} \quad \text{and} \quad \mathbf{g}_{2_{i+\frac{1}{2}}} = \mathbf{g}_{2_{i+1}}. \quad (22)$$

A *second-order scheme*, in space, is achieved by applying van Leer's MUSCL scheme to the k -th components of \mathbf{g}_1 and \mathbf{g}_2 as

$$g_{1_{i+\frac{1}{2}}}^{(k)} = g_{1_i}^{(k)} + \frac{1}{2}\Delta x s_i^+ \quad (23)$$

$$g_{2_{i+\frac{1}{2}}}^{(k)} = g_{2_{i+1}}^{(k)} - \frac{1}{2}\Delta x s_{i+1}^- \quad (24)$$

where s_i^+ and s_i^- are respectively, the slopes of $g_1^{(k)}$ and $g_2^{(k)}$ on the control volume I_i . These slopes are defined as

$$s_i^\pm = \frac{1}{\Delta x} (g_{1,2_{i+1}}^{(k)} - g_{1,2_i}^{(k)}) \phi(\theta_i^\pm), \quad \theta_i^\pm = \frac{g_{1,2_i}^{(k)} - g_{1,2_{i-1}}^{(k)}}{g_{1,2_{i+1}}^{(k)} - g_{1,2_i}^{(k)}} \quad (25)$$

where $\phi(\theta)$ defines the van Leer's slope limiter function

$$\phi = \frac{|\theta| + \theta}{1 + |\theta|}. \quad (26)$$

Other limiter functions can also be applied in the sense of [54]. Note that, in the case the slopes $s^\pm = 0$ or $\phi = 0$, the MUSCL scheme reduces to the first-order upwind scheme. Once the $\mathbf{g}_{1_{i\pm\frac{1}{2}}}$ and $\mathbf{g}_{2_{i\pm\frac{1}{2}}}$ values have been computed, the numerical fluxes for $\mathbf{u}_{i\pm\frac{1}{2}}$ and $\mathbf{v}_{i\pm\frac{1}{2}}$ can be obtained from (19).

4.1. WENO reconstruction for spatial discretization

Next, we apply the well known WENO-type interpolant approach where the approximate solution is reconstructed by higher-order polynomials, compared to the linear ones in the MUSCL approach. Applying this reconstruction directly to the k -th components of the characteristic variables $\mathbf{g}_{1,2} = \mathbf{v} \pm \mathbf{C}\mathbf{u}$ gives a non-oscillatory higher-order discretization in space. In the present work, we apply the improved fifth-order WENO reconstruction proposed in [8]. For this scheme, the discrete values of each component of $\mathbf{g}_{1_{i+\frac{1}{2}}}$ and $\mathbf{g}_{2_{i+\frac{1}{2}}}$, at a cell boundary $i + \frac{1}{2}$, are defined as left and right extrapolated values $\mathbf{g}_{1_{i+\frac{1}{2}}}^L$ and $\mathbf{g}_{2_{i+\frac{1}{2}}}^R$ i.e.

$$\mathbf{g}_{1_{i+\frac{1}{2}}} = \mathbf{g}_{1_{i+\frac{1}{2}}}^L \quad \text{end} \quad \mathbf{g}_{2_{i+\frac{1}{2}}} = \mathbf{g}_{2_{i+\frac{1}{2}}}^R. \quad (27)$$

For a generic function $\psi(x)$ the *fifth-order accurate* left boundary extrapolated value $\psi_{i+\frac{1}{2}}^L$ is defined as

$$\psi_{i+\frac{1}{2}}^L = \sum_{r=0}^2 \omega_r^- h_r^- \quad (28)$$

where h_r^- are extrapolated values obtained from cell averages in the r th stencil $(i-r, i-r+1, i-r+2)$

as

$$\begin{aligned} h_0^- &= \frac{1}{3}\psi_i + \frac{5}{6}\psi_{i+1} - \frac{1}{6}\psi_{i+2}; \\ h_1^- &= -\frac{1}{6}\psi_{i-1} + \frac{5}{6}\psi_i + \frac{1}{3}\psi_{i+1}; \\ h_2^- &= \frac{1}{3}\psi_{i-2} - \frac{7}{6}\psi_{i-1} + \frac{11}{6}\psi_i, \end{aligned}$$

and ω_r^- , $r = 0, 1, 2$ are non-linear WENO weights given by

$$\omega_r^- = \frac{a_r}{\sum_{l=0}^2 a_l}, \quad a_r = C_r \left(1 + \frac{\eta_5}{IS_r^- + \varepsilon} \right), \quad r = 0, 1, 2 \quad (29)$$

with $C_0 = 3/10$, $C_1 = 3/5$, $C_2 = 1/10$, and ε is a very small number introduced to guarantee that the denominator does not vanish and is set to $\varepsilon = 10^{-40}$ in our numerical simulations, as suggested in [8]. The smoothness indicators IS_r^- are given by

$$\begin{aligned} IS_0^- &= \frac{13}{12}(\psi_i - 2\psi_{i+1} + \psi_{i+2})^2 + \frac{1}{4}(3\psi_i - 4\psi_{i+1} + \psi_{i+2})^2; \\ IS_1^- &= \frac{13}{12}(\psi_{i-1} - 2\psi_i + \psi_{i+1})^2 + \frac{1}{4}(\psi_{i-1} - \psi_{i+1})^2; \\ IS_2^- &= \frac{13}{12}(\psi_{i-2} - 2\psi_{i-1} + \psi_i)^2 + \frac{1}{4}(\psi_{i-2} - 4\psi_{i-1} + 3\psi_i)^2. \end{aligned}$$

The expression η_5 is given in terms of the smoothness indicators as

$$\eta_5 = |IS_0^- - IS_2^-|.$$

The right face value $\psi_{i+\frac{1}{2}}^R$ is given by symmetry as

$$\psi_{i+\frac{1}{2}}^R = \sum_{r=0}^2 \omega_r^+ h_r^+ \quad (30)$$

where now

$$\begin{aligned} h_0^+ &= \frac{1}{3}\psi_{i+3} - \frac{7}{6}\psi_{i+2} + \frac{11}{6}\psi_{i+1}; \\ h_1^+ &= -\frac{1}{6}\psi_{i+2} + \frac{5}{6}\psi_{i+1} + \frac{1}{3}\psi_i; \\ h_2^+ &= \frac{1}{3}\psi_{i+1} + \frac{5}{6}\psi_i - \frac{1}{6}\psi_{i-1}. \end{aligned}$$

The corresponding weights ω_r^+ and smoothness indicators are given by (29) with

$$\begin{aligned} IS_0^+ &= \frac{13}{12}(\psi_{i+1} - 2\psi_{i+2} + \psi_{i+3})^2 + \frac{1}{4}(3\psi_{i+1} - 4\psi_{i+2} + \psi_{i+3})^2; \\ IS_1^+ &= \frac{13}{12}(\psi_i - 2\psi_{i+1} + \psi_{i+2})^2 + \frac{1}{4}(\psi_i - \psi_{i+2})^2; \\ IS_2^+ &= \frac{13}{12}(\psi_{i-1} - 2\psi_i + \psi_{i+1})^2 + \frac{1}{4}(\psi_{i-1} - 4\psi_i + 3\psi_{i+1})^2. \end{aligned}$$

Once the above reconstructions (28) and (30) have been applied to each component of the characteristic variables form (27) (and in a similar way for the face values a cell boundary $i - \frac{1}{2}$), the numerical fluxes for $\mathbf{u}_{i\pm\frac{1}{2}}$ and $\mathbf{v}_{i\pm\frac{1}{2}}$ are obtained from (19), as for the lower-order cases.

Remark 2. A small modification on the formula of the weights (29) has been proposed in [8] to recover fifth-order accuracy at a first-order critical point. The new weights are defined as

$$\omega_r^- = \frac{a_r}{\sum_{l=0}^2 a_l}, \quad a_r = C_r \left(1 + \left(\frac{\eta_5}{IS_r^- + \varepsilon} \right)^q \right), \quad r = 0, 1, 2 \quad (31)$$

and with $q = 2$ fifth-order is achieved at a first-order critical point. From a practical point of view, increasing q decreases the relative importance of the discontinuous stencil, making the scheme slightly more dissipative. Moreover, we have found that this may also have a stabilizing effect in critical points on discontinuities as can be seen, for example, in Fig 1. However, in the numerical results presented in subsequent sections, $q = 1$ has been implemented, unless otherwise stated.

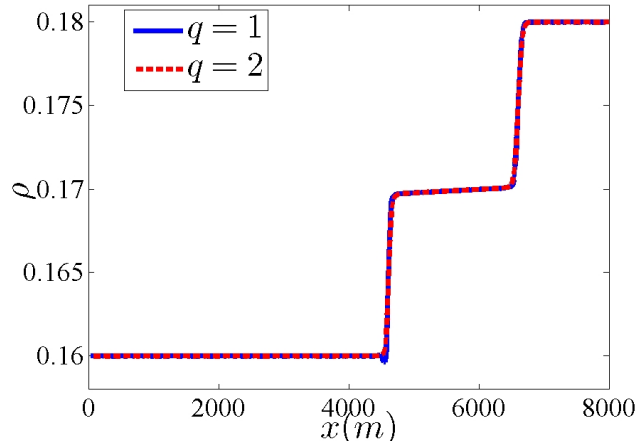


Figure 1: Comparison of using the different weight values from (29) and (31)

Remark 3. The approximations of the flux function $\mathbf{f}(\mathbf{u})_i$ and source term $\mathbf{s}(\mathbf{u})_i$ in (20) can be

performed by using Simpson's quadrature rule as in [50, 14], for example. However, for small values of the relaxation rate ϵ , it suffices to project $\mathbf{f}(\mathbf{u})_i$ and $\mathbf{s}(\mathbf{u})_i$ into the local equilibriums $\mathbf{f}(\mathbf{u}_i)$ and $\mathbf{s}(\mathbf{u}_i)$, respectively.

4.2. Implicit-explicit methods for time integration

The semi-discrete relaxation system (20) can be reformulated as a system of autonomous ordinary differential equations as

$$\frac{d\mathcal{Y}}{dt} = \mathcal{F}(\mathcal{Y}) - \frac{1}{\epsilon}\mathcal{G}(\mathcal{Y}), \quad (32)$$

with the time-dependent vector functions given as

$$\mathcal{Y} = \begin{pmatrix} \mathbf{u}_i \\ \mathbf{v}_i \end{pmatrix}, \quad \mathcal{F}(\mathcal{Y}) = \begin{pmatrix} \mathbf{s}(\mathbf{u})_i - \mathcal{D}_x \mathbf{v}_i \\ -\mathbf{C}^2 \mathcal{D}_x \mathbf{u}_i \end{pmatrix} \quad \text{and} \quad \mathcal{G}(\mathcal{Y}) = \begin{pmatrix} 0 \\ \mathbf{v}_i - \mathbf{f}(\mathbf{u})_i \end{pmatrix},$$

with

$$\mathcal{D}_x \mathbf{v}_i = \frac{\mathbf{v}_{i+\frac{1}{2}} - \mathbf{v}_{i-\frac{1}{2}}}{\Delta x} \quad \text{and} \quad \mathcal{D}_x \mathbf{u}_i = \frac{\mathbf{u}_{i+\frac{1}{2}} - \mathbf{u}_{i-\frac{1}{2}}}{\Delta x}.$$

When $\epsilon \rightarrow 0$, system (32) becomes stiff and an explicit treatment of the right-hand side will require small time steps that may restrict application to any long time simulations. Integrating system (32) by an implicit scheme, either linear or nonlinear algebraic equations have to be solved at every time step of a simulation. This can be computationally demanding. To alleviate these problems, we consider a time marching approach based on implicit-explicit (IMEX) Runge-Kutta (RK) splitting. The non-stiff stage of the splitting in $\mathcal{F}(\mathcal{Y})$ is treated by an explicit RK scheme, while the stiff stage for $\mathcal{G}(\mathcal{Y})$ by a diagonally implicit RK (DIRK) scheme, we refer to [3, 48] for more details.

By denoting with Δt^n the current time step and \mathcal{Y}^n the approximate solution at time $t = t_n$, the implementation of the s -stage IMEX method to solve (32) can be carried out as follows

$$\mathcal{Y}_k = \mathcal{Y}^n + \Delta t^n \sum_{m=1}^{k-1} \tilde{a}_{km} \mathcal{F}(\mathcal{Y}_m) - \frac{\Delta t^n}{\epsilon} \sum_{m=1}^s a_{km} \mathcal{G}(\mathcal{Y}_m), \quad k = 1, 2, \dots, s \quad (33)$$

$$\mathcal{Y}^{n+1} = \mathcal{Y}^n + \Delta t^n \sum_{k=1}^s \tilde{b}_k \mathcal{F}(\mathcal{Y}_k) - \frac{\Delta t^n}{\epsilon} \sum_{k=1}^s b_k \mathcal{G}(\mathcal{Y}_k). \quad (34)$$

The $s \times s$ matrices $\tilde{\mathbf{A}} = [\tilde{a}_{km}]$, \tilde{a}_{km} for $m \geq k$ and $\mathbf{A} = [a_{km}]$ are chosen such that the resulting splitting is explicit in $\mathcal{F}(\mathcal{Y})$ and implicit in $\mathcal{G}(\mathcal{Y})$. The s -vectors $\tilde{\mathbf{b}}$ and \mathbf{b} are the canonical coefficients which characterize the IMEX RK scheme [48]. They can be given in a standard double tableau in Butcher notation as

$$\begin{array}{c|c} \tilde{\mathbf{c}} & \tilde{\mathbf{A}} \\ \hline & \tilde{\mathbf{b}}^T \end{array} \quad \text{and} \quad \begin{array}{c|c} \mathbf{c} & \mathbf{A} \\ \hline & \mathbf{b}^T \end{array}$$

where $\tilde{\mathbf{c}}$ and \mathbf{c} are the s -vectors used in the context of non-autonomous systems. The left and right tables are associated with the explicit and implicit RK schemes, respectively.

For *second-order time integration* (combined with the MUSCL scheme) the tables are given by

$$\begin{array}{c|cc} 0 & 0 & 0 \\ 1 & 1 & 0 \\ \hline & \frac{1}{2} & \frac{1}{2} \end{array} \quad \text{and} \quad \begin{array}{c|cc} -1 & -1 & 0 \\ 2 & 1 & 1 \\ \hline & \frac{1}{2} & \frac{1}{2} \end{array}$$

The splitting treats, alternatively, the stiff source terms implicitly in two steps (where due to linearity of \mathbf{v} one still solves them explicitly), and the convection terms with two explicit steps. Thus, we have an explicit implementation of an implicit source term, with stability constraints solely determined by the non-stiff advection terms, just as in a usual finite volume scheme.

In this work we use the *third-order IMEX method* studied in [3] with the WENO discretization. Its corresponding double tableau is given as

$$\begin{array}{c|ccc} 0 & 0 & 0 & 0 \\ \gamma & \gamma & 0 & 0 \\ 1-\gamma & \gamma-1 & 2-2\gamma & 0 \\ \hline & 0 & \frac{1}{2} & \frac{1}{2} \end{array} \quad \text{and} \quad \begin{array}{c|ccc} 0 & 0 & 0 & 0 \\ \gamma & 0 & \gamma & 0 \\ 1-\gamma & 0 & 1-2\gamma & \gamma \\ \hline & 0 & \frac{1}{2} & \frac{1}{2} \end{array}$$

with $\gamma = (3 + \sqrt{3})/6$. Similar to the previous method, using the above IMEX scheme neither linear algebraic equations nor non-linear source terms can arise. Further, since the source terms are treated implicitly and the advection terms are treated explicitly, the high-order relaxation schemes are stable independently of ϵ , so the choice of Δt^n in each time step of a simulation is based only on the usual CFL conditions [34],

$$CFL = \max \left(\left(\max_{i,k} c_k^n \right) \frac{\Delta t^n}{\Delta x}, \frac{\Delta t^n}{\Delta x} \right) \leq 1,$$

for the first-order scheme, and

$$CFL = \max \left(\left(\max_{i,k} c_k^n \right) \frac{\Delta t^n}{\Delta x}, \frac{\Delta t^n}{\Delta x} \right) \leq \frac{1}{2},$$

for the higher-order schemes where the values of the relaxation constants c_k^n are evaluated in each time step as presented in Section 4.4.

We note that, in the limit $\epsilon \rightarrow 0$, the time integration procedure (33)-(34) tends to a TVD time integration scheme of the limit equations based on the explicit scheme given by the left tableau.

Remark 4. *The relaxation rate ϵ influences both the regularization effect of the scheme and its accuracy in smooth regions of the flow. It can be viewed as viscosity coefficient such that more numerical diffusion is added for larger values of ϵ . Only in the case that $\Delta t^n = O(\epsilon)$ the scheme goes unstable being inconsistent to the relaxation system (15). However, here we present a numerical scheme that under-resolves (15) in the regime $\Delta t^n \gg \epsilon$ and thus will never break down in our case.*

4.3. Initial and boundary conditions

For a given initial data $\mathbf{u}_0(x)$, we choose the initial conditions for the relaxation system presented above as

$$\begin{aligned}\mathbf{u}(x, 0) &= \mathbf{u}_0(x), \\ \mathbf{v}(x, 0) &= \mathbf{v}_0(x) \equiv \mathbf{f}(\mathbf{u}_0(x)).\end{aligned}$$

In the small relaxation limit ($\epsilon \rightarrow 0^+$), the relaxation system presented in (15) satisfies initially the above local equilibrium hence, in order to avoid the introduction of an initial layer through the relaxation system, the above initial value for \mathbf{v} is chosen.

For the boundary conditions, given a physical boundary conditions, \mathbf{u}_p , that may be imposed in a problem, we set $\mathbf{v}_p = \mathbf{f}(\mathbf{u}_p)$ so as to avoid the introduction of artificial boundary layers. For instance, if Dirichlet boundary conditions are imposed to the original nonlinear system, in a spatial computational domain $[a, b]$, as

$$\mathbf{u}(a, t) = \mathbf{u}_a(t), \quad \text{and} \quad \mathbf{u}(b, t) = \mathbf{u}_b(t), \quad t > 0,$$

then, the boundary conditions for the relaxation variable \mathbf{v} are given by

$$\mathbf{v}(a, t) = \mathbf{f}(\mathbf{u}_a(t)), \quad \mathbf{v}(b, t) = \mathbf{f}(\mathbf{u}_b(t)), \quad t > 0.$$

If instead, \mathbf{u} satisfies the homogeneous Neumann boundary condition

$$\frac{\partial \mathbf{u}}{\partial x} \Big|_{x=a} = 0, \quad \text{and} \quad \frac{\partial \mathbf{u}}{\partial x} \Big|_{x=b} = 0, \quad t > 0$$

then, since

$$\frac{\partial \mathbf{v}}{\partial x} = \mathbf{f}'(\mathbf{u}) \frac{\partial \mathbf{u}}{\partial x}$$

boundary conditions for the relaxation system (15) are derived as

$$\frac{\partial \mathbf{v}}{\partial x} \Big|_{x=a} = 0 \quad \text{and} \quad \frac{\partial \mathbf{v}}{\partial x} \Big|_{x=b} = 0, \quad t > 0.$$

Periodic boundary conditions which are given by $\mathbf{u}(a, t) = \mathbf{u}(b, t)$, can be easily imposed in the relaxation variables as $\mathbf{v}(a, t) = \mathbf{v}(b, t) = \mathbf{f}(\mathbf{u}(a, t))$. In general, any choice that leads at the limit to the associated boundary and initial equilibrium can be used.

From a practical point of view, and at the discrete level, an easy way to impose the boundary conditions in the numerical schemes is to use ghost cells; that is, to extend the computational domain by extra grid cells along the boundaries, whose values are set, based on the imposed boundary conditions, at the beginning of each time step (in the RK solver). We refer to [37] for a thorough discussion of their implementation within the finite volume framework.

4.4. On the choice of characteristic speeds

An important matter, from a practical point of view, is the choice of the relaxation characteristic speeds in \mathbf{C}^2 so as to satisfy the criterion (11). The size of \mathbf{C}^2 has also a decisive influence regarding the numerical dissipation associated with the numerical schemes derived from (9). For both computational and theoretical purposes it is sometimes necessary to choose \mathbf{C}^2 to have distinct diagonal elements so as to avoid the degeneracy in the relaxation system. The construction of \mathbf{C}^2 must then be based on rough estimates of the characteristic speeds of the original problem. Hence, we can set, for example, every eigenvalue λ of $\mathbf{f}'(\mathbf{u})$ to satisfy $|\lambda| \leq c_{\max}$, where $c_{\max} = \max_k c_k$. By doing so we ensure that the characteristic speeds of the hyperbolic part of (9) are at least as large as the characteristic speeds of the original problem.

In our implementation, the values of $c_k, k = 1, \dots, n$ ($n = 2$ for the traffic flow models), are adjusted according to the solutions behavior by considering a global selection on every time step Δt^n . Based on the global maximum of each eigenvalue of the system's Jacobian matrices over the grid cells I_i , their choice is made as follows

$$c_k^n = \max_i |\lambda_k^n| + e, \quad k = 1, \dots, n.$$

where e is a small correction parameter of $O(10^{-2})$, added to avoid the characteristic speeds from vanishing. Another choice is to calculate the speeds c_k locally on every cell I_i [6, 52] by setting

$$c_k^n|_i = \max_k |\lambda_k^n|_i + e, \quad k = 1, \dots, n$$

We note that larger values for the c_k usually add more numerical viscosity, so for accuracy reasons it is desirable to have c_k as small as possible. The first choice for calculating the characteristic speeds was proven sufficient for our calculations in the next sections.

5. Numerical results and discussion

In this section extensive numerical tests and results are presented for all traffic models presented in Section 2. Characteristic benchmark problems are considered to assess the performance of the proposed high-order relaxations schemes. For all numerical tests presented next, the relaxation rate ϵ was set to 10^{-8} and all other computational parameters were those presented in Section 4.

5.1. Numerical tests for the PW traffic model

In this section we numerically solve the PW model with four different initial conditions for the Riemann problem (3). It is well-known, see for example [61], that the PW model admits eight types of wave solutions to the Riemann problem (RP), including four first-order waves and four second-order waves. The four first-order wave solutions are a 1-shock wave (S_1), a 2-shock wave (S_2), a 1-rarefaction (R_1) and a 2-rarefaction (R_2), each one associated with the first characteristic and the other with the second characteristic of the model. The four second-order wave solutions

are a $S_1 - S_2$ (left S_1 and right S_2), a $R_1 - R_2$ (left R_1 and right R_2), a $R_1 - S_2$ (left R_1 and right S_2) wave and an $S_1 - R_2$ (left S_1 and right R_2).

Setting the unit length and time to $\tilde{l} = 10m$ and $\tilde{\tau} = 10s$, the following four initial jump conditions are considered here in a road of length $L = 8000m$.

[RP1] A problem that has $R_1 - R_2$ wave solutions with

$$\rho(x, 0) = 0.16, \quad (35)$$

$$u(x, 0) = \begin{cases} u_l = V^e(0.16), & \text{for } x \leq 4000, \\ u_r = V^e(0.16) + 0.2 & \text{for } x > 4000. \end{cases} \quad (36)$$

[RP2] A problem that has $R_1 - S_2$ wave solutions with

$$\rho(x, 0) = \begin{cases} \rho_l = 0.16, & \text{for } x \leq 4000, \\ \rho_r = 0.16 - 0.02, & \text{for } x > 4000, \end{cases} \quad (37)$$

$$u(x, 0) = V^e(0.16). \quad (38)$$

[RP3] A problem that has $S_1 - S_2$ wave solutions with

$$\rho(x, 0) = 0.16, \quad (39)$$

$$u(x, 0) = \begin{cases} v_l = V^e(0.16), & \text{for } x \leq 4000, \\ u_r = V^e(0.16) - 0.2, & \text{for } x > 4000. \end{cases} \quad (40)$$

[RP4] A problem that has $S_1 - R_2$ wave solutions with

$$\rho(x, 0) = \begin{cases} \rho_l = 0.16, & \text{for } x \leq 4000, \\ \rho_r = 0.16 + 0.02 & \text{for } x > 4000, \end{cases} \quad (41)$$

$$u(x, 0) = V^e(0.16). \quad (42)$$

Two different cases are considered for each RP. Setting the final simulation time to $T_f = 1000s$, the first case is for relaxation time $\tau = 1000\tilde{\tau}$ and the second case for $\tau = 5\tilde{\tau}$. In the first case the relaxation time is big enough for us to watch the evolution of the four different types of second-order waves, which consist of two elementary waves, until time T_f . In the second case, where the relaxation time is much shorter, 2-waves relax to 1-waves and free and clustered regions are formed, due to the effect of the source term.

In the numerical results presented next, we compare the ability of the relaxation schemes, namely the first-order upwind, second-order MUSCL and fifth-order WENO, to describe the evolution of these elementary waves, as well as the source terms effects. In all numerical results the number of grid points used was set to $npts = 400$, producing a relatively sparse mesh, the CFL

value was 0.4 for the higher-order schemes and 0.9 for the upwind one, and homogeneous Neumann boundary conditions were implemented.

The numerical results obtained for RP1 are presented in Fig. 2, where the spatio-temporal evolutions of the density and velocity until time T_f are shown. In Fig. 3 a comparison of the numerical results obtained with the different schemes for the two rarefaction waves at $t = 500s$ is shown. As it can be seen, the higher-order schemes are able to produce accurate solutions with high-resolution, compared to the upwind one which is highly diffusive. Comparing the MUSCL and WENO schemes, a better resolution of the waves can be seen for the WENO scheme.

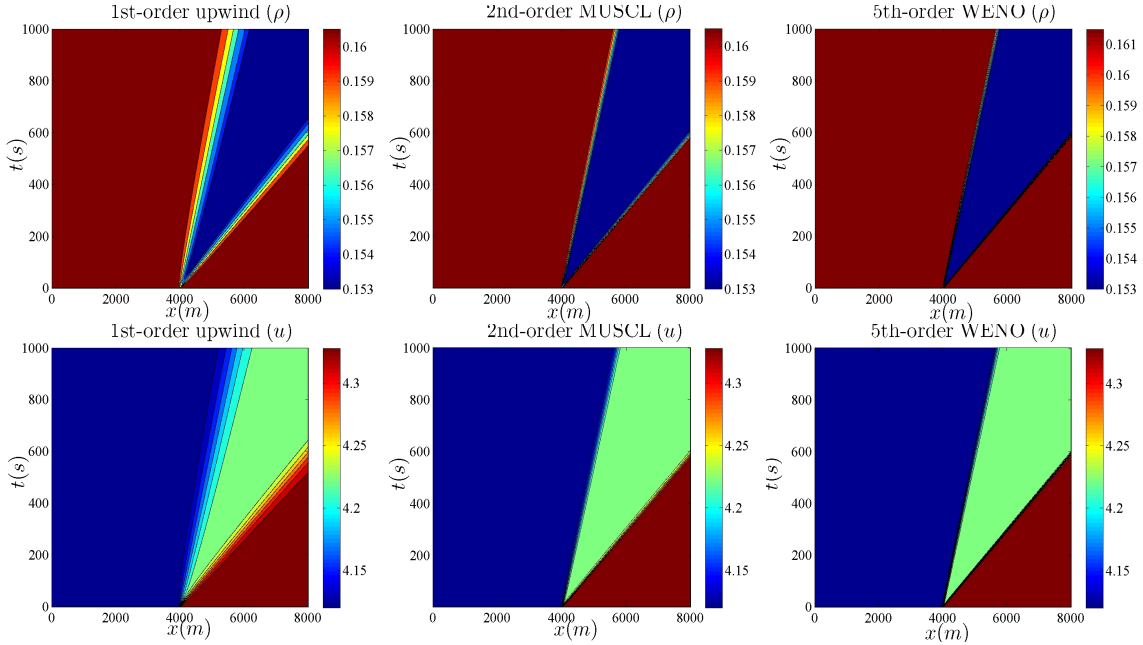


Figure 2: PW model: $R_1 - R_2$ wave solutions for RP1 for ρ (top) and u

For RP2, results are presented in Figs 4 and 5. Again, the superiority of the high-resolution schemes is evident, compared to the upwind one. Since this solution contains a shock, it is important to note that, for the high-resolution schemes, no un-physical oscillations are appearing in the numerical results, and the numerical solution remains stable in its evolution. The same observation holds for the results for RP3 and RP4 in Figs. 6 and 7, respectively. There, an $S_1 - S_2$ and an $S_1 - R_2$ solution are presented for the high-resolution schemes. Again non-oscillatory solutions of the shock waves are computed for both schemes, with the WENO scheme providing better resolution for both test cases.

Next, the second case for $\tau = 5\tilde{\tau}$ is considered for all Riemann problems. For RP1 the spatio-temporal results for the density and velocity are shown in Fig. 8, for all schemes. In this case, at around $t = 5\tau$, a downstream shock S_1 forms when the traffic conditions relax to equilibrium

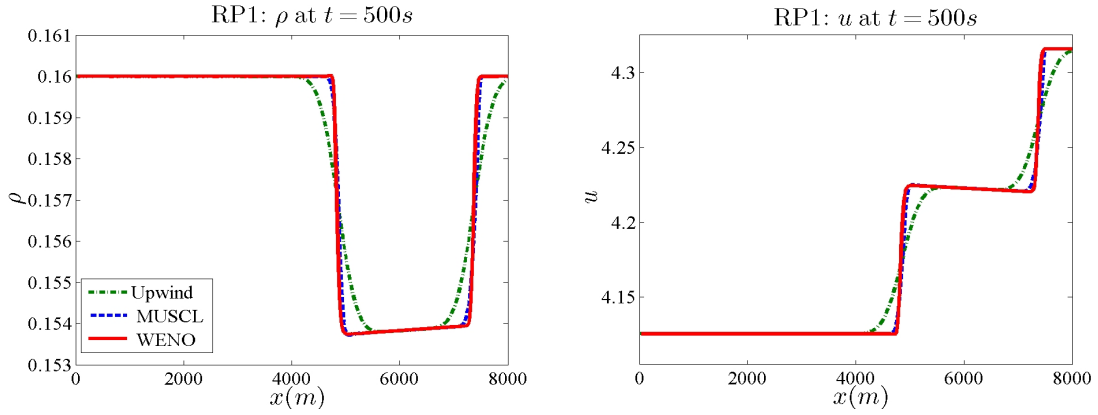


Figure 3: PW model: $R_1 - R_2$ wave solutions for RP1 at $t = 500s$

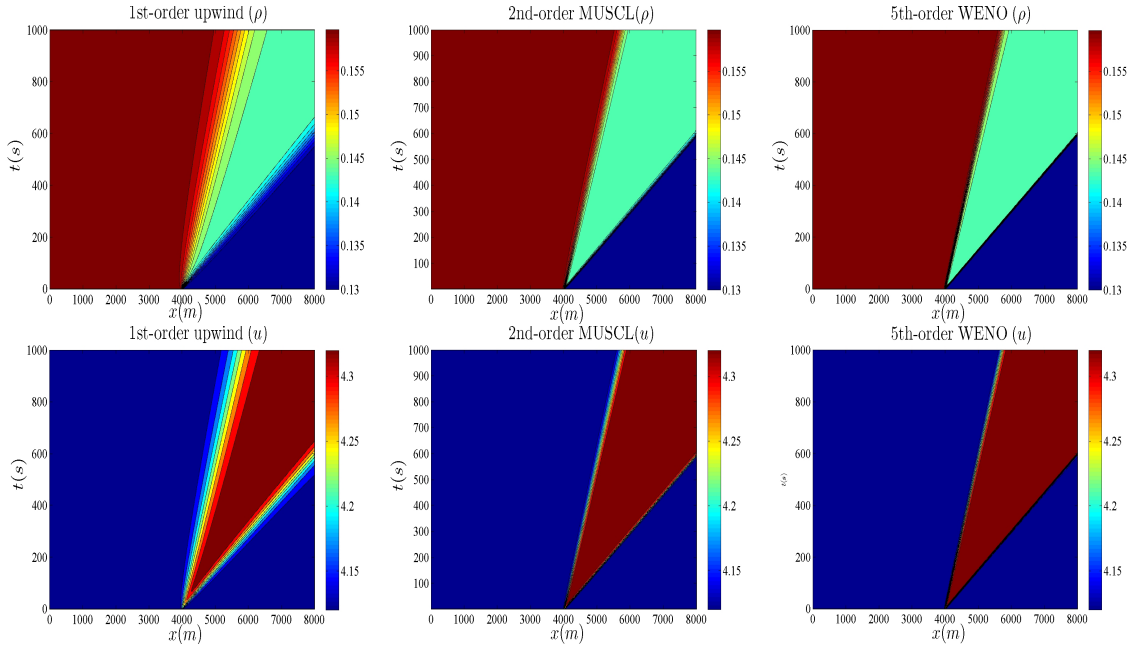


Figure 4: PW model: $R_1 - S_2$ wave solutions for RP2 for ρ (top) and u

($u = V^e(0.16)$). After that, a free-flow region with lower density and higher travel speed is formed. The free-flow region travels with speed λ_* and eventually disappears as the waves propagate, and the flow finally will become uniform. It can be observed that the fine details of the flow cannot be predicted by the first-order scheme, while the higher-order schemes produce a sharp resolution.

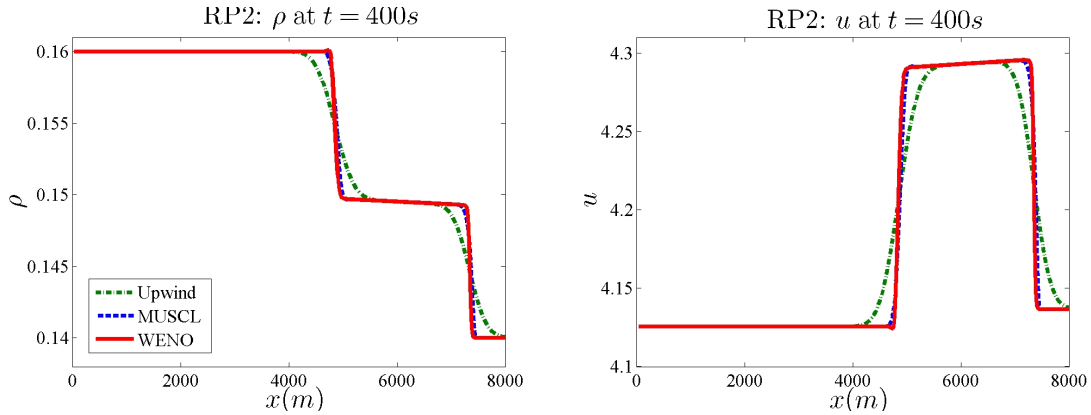


Figure 5: PW model: $R_1 - S_2$ wave solutions for RP2 at $t = 400s$

The WENO scheme provides more accurate results at the initial stages of the traffic evolution. This is also evident from Fig. 9 where the evolution of the traffic flow rate $q = u\rho$ is presented.

For RP2 the numerical solution with the high-order schemes is shown in Figs 10 and 11. In this situation, a new R_1 wave forms when the S_2 wave disappears. Both schemes can predict this transition and the propagation of the two rarefaction waves. Similar to the previous case, the WENO scheme can provide sharper resolution and fine details on the flow, on the same grid used.

With the initial conditions for RP3, the numerical solutions for the MUSCL and WENO schemes are presented in Figs 12 and 13. In this situation, at around $t = 5\tau$, the S_2 wave disappears and an R_1 wave forms. After that, a cluster with higher vehicle density is formed that travels with speed λ_* . As the waves propagate, traffic conditions become uniform in later times. The cluster formation and propagation is well predicted by both high-order schemes which provide stable non-oscillatory solutions. Again, the WENO resolution is moderately better than that of the MUSCL one.

The final case is for RP4 where now the R_2 wave disappears and a new S_1 shock wave is formed. The resulted numerical solutions are displayed in Figs 14 and 15. Again the formation and propagation of the resulted waves are well resolved by the high-order schemes, with the WENO relaxation scheme providing sharper results for the shock waves.

5.2. Numerical tests for the AR and ARZ traffic models

Contrary to the PW model, the λ_2 eigenvalue for the AR and ARZ traffic models is linearly degenerate and therefore a contact discontinuity (C_2) is admissible in their elementary wave structure. Hence, depending on the data, the wave related with the first characteristic speed is either a rarefaction R_1 or shock S_1 and that related to the second speed is a contact discontinuity.

First, numerical tests and results for the AR model are presented. In all numerical results $L = 16m$, $T_f = 6s$ and the number of grid points used was set to $n_{pts} = 400$, unless otherwise

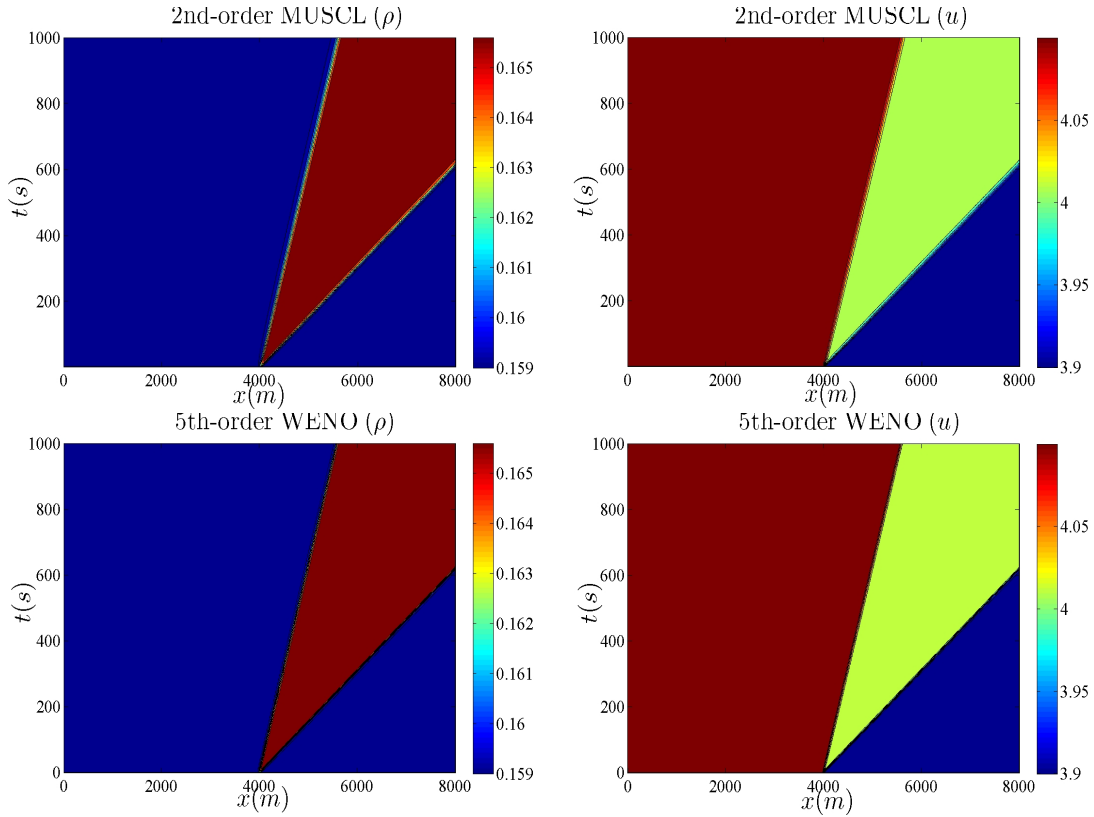


Figure 6: PW model: $S_1 - S_2$ wave solutions for RP3 for ρ (top) and u

stated. Comparison with the corresponding analytical solutions, [2], for each numerical test are also presented.

AR: Case 1. The initial condition for this problem is

$$[\rho(x, 0), u(x, 0)] = \begin{cases} [\rho_l, u_l] = [0.5, 0.6], & \text{for } x \leq 8, \\ [\rho_r, u_r] = [0.8, 0.4], & \text{for } x > 8 \end{cases} \quad (43)$$

and the exact solution of this Riemann problem is a shock traveling with negative speed followed by a contact discontinuity moving to the right with the speed of the leading cars $u_r = 0.4$. The spatio-temporal evolution of the numerical solution for the WENO scheme is presented in Fig. 16. Comparison with the exact solution for all schemes is presented in Fig. 17. As it can be seen, all schemes reproduce the correct solution, with the upwind one being the most diffusive, especially in the contact discontinuity resolution, and with the WENO scheme being the most accurate one.

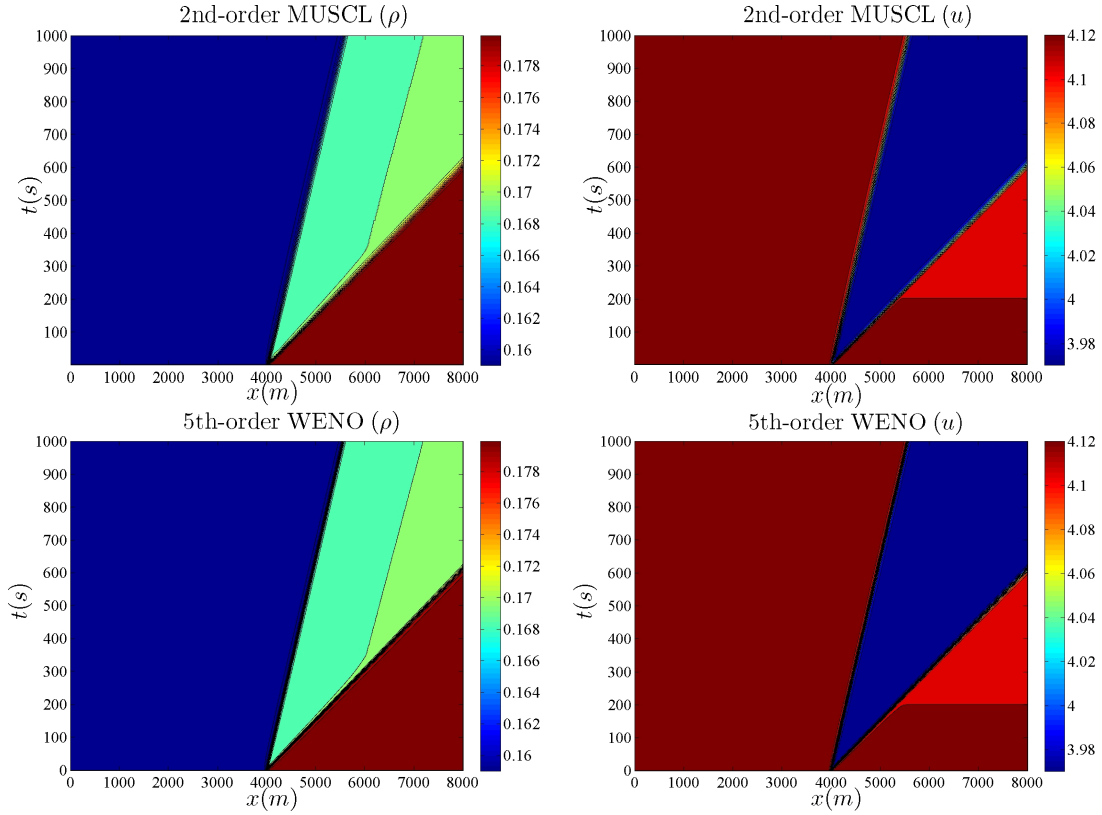


Figure 7: PW model: $S_1 - R_2$ wave solutions for RP4 for ρ (top) and u

AR: Case 2. The initial condition for this problem is

$$[\rho(x, 0), u(x, 0)] = \begin{cases} [\rho_l, u_l] = [0.8, 0.6], & \text{for } x \leq 8, \\ [\rho_r, u_r] = [0.6, 1], & \text{for } x > 8. \end{cases} \quad (44)$$

The exact solution here is a rarefaction wave followed by a contact discontinuity moving to the right with maximum speed $u_r = 1$. The spatio-temporal evolution of the numerical solution for the MUSCL and WENO schemes is presented in Fig. 18, while comparison with the exact solution for all schemes is presented in Fig. 19. The contact discontinuity is well resolved by the higher order schemes with the WENO scheme, again, exhibiting the better resolution of the wave structured.

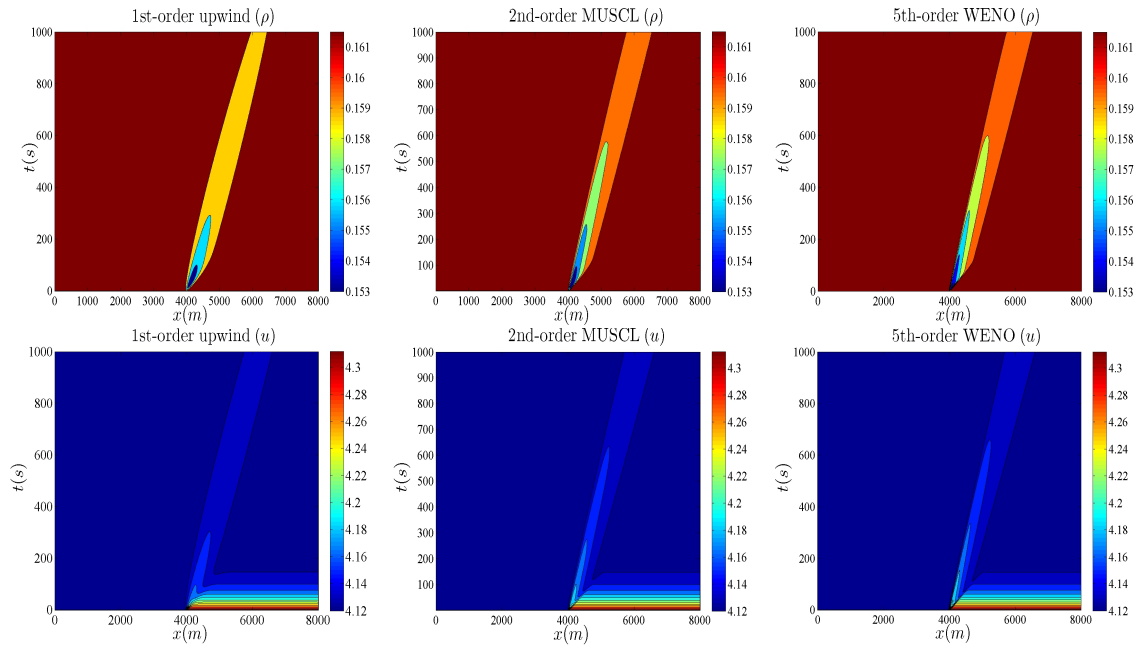


Figure 8: PW model: Formation of a free-flow region for RP1

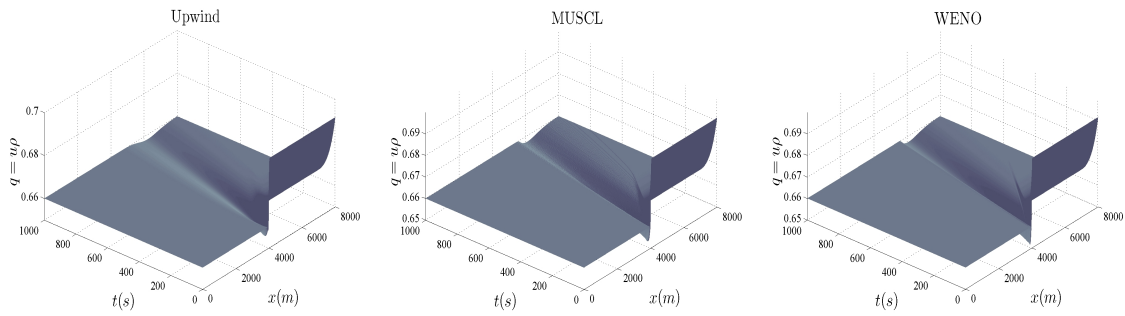


Figure 9: PW model: Formation of a free region for RP1, solutions' evolution for q

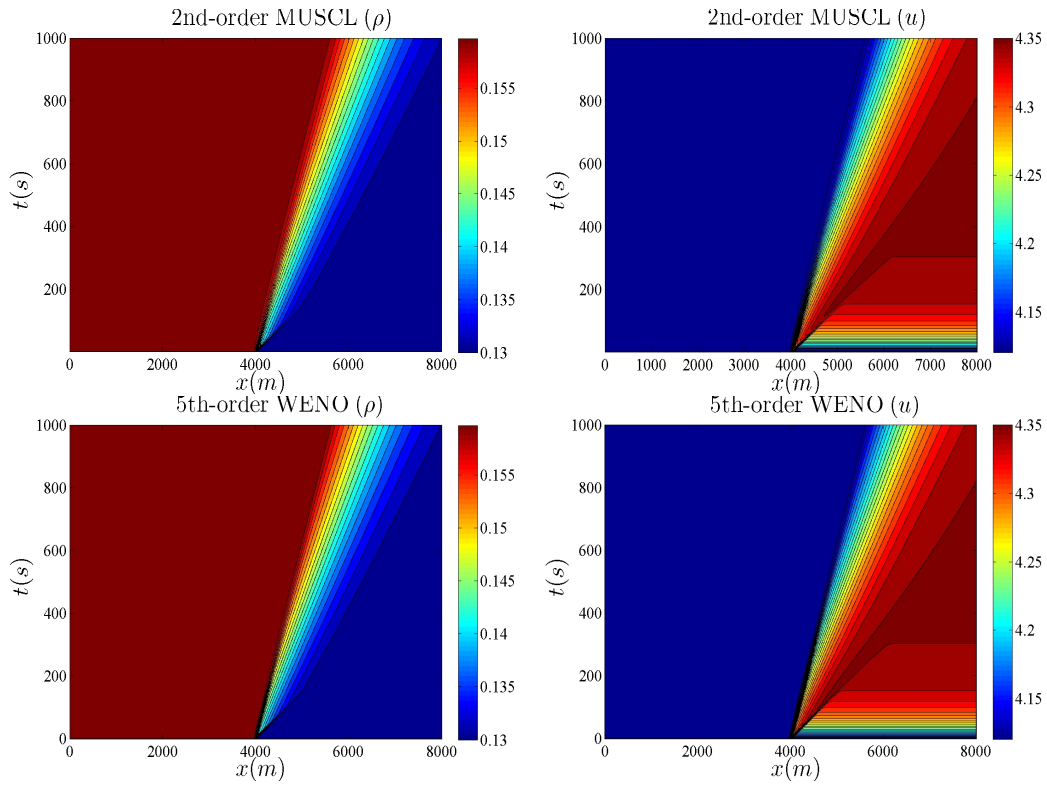


Figure 10: PW model: Formation of two rarefaction waves for RP2

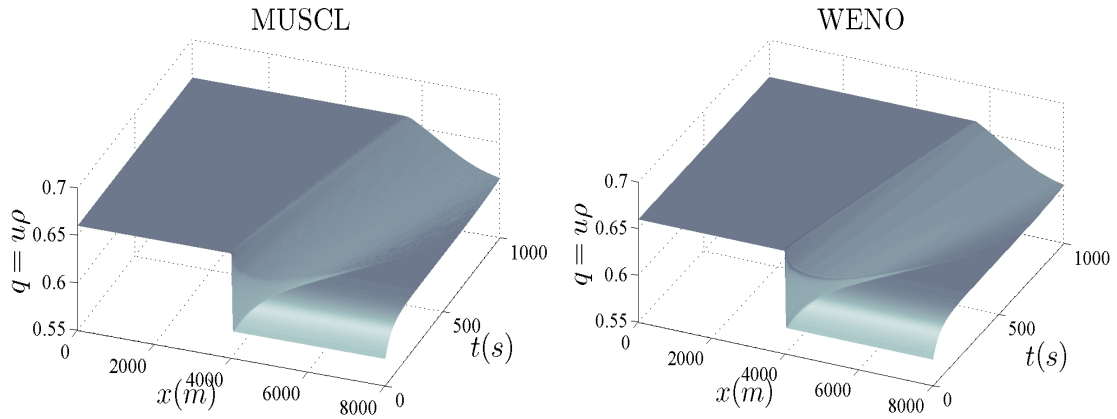


Figure 11: PW model: Formation of two rarefaction waves for RP2, solutions' evolution for q

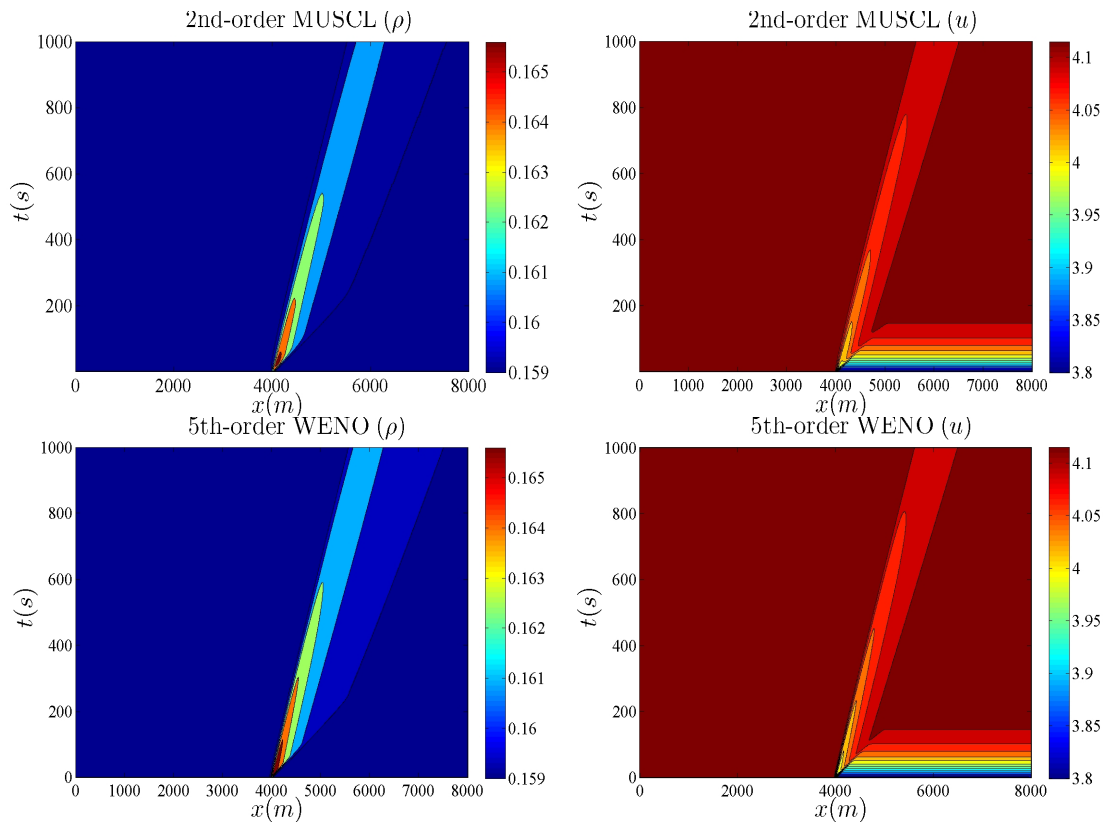


Figure 12: PW model: Formation of a cluster for RP3

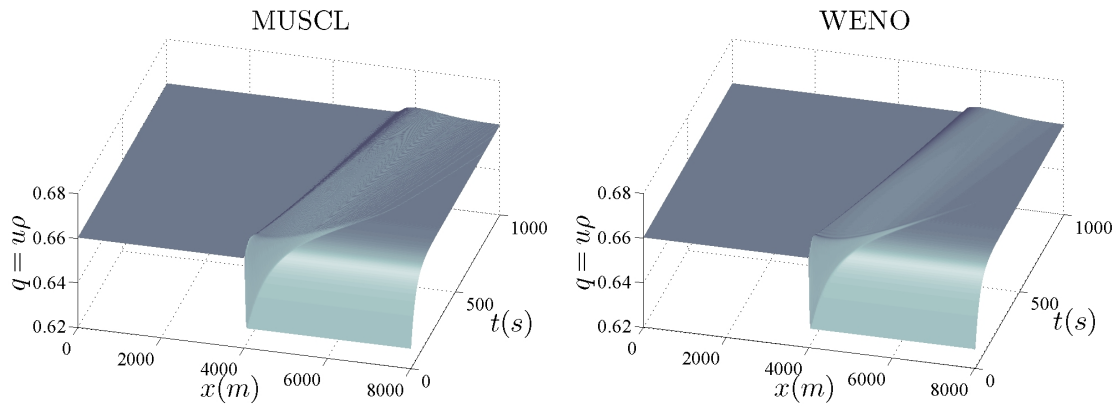


Figure 13: PW model: Formation of a cluster for RP3, solutions' evolution for q

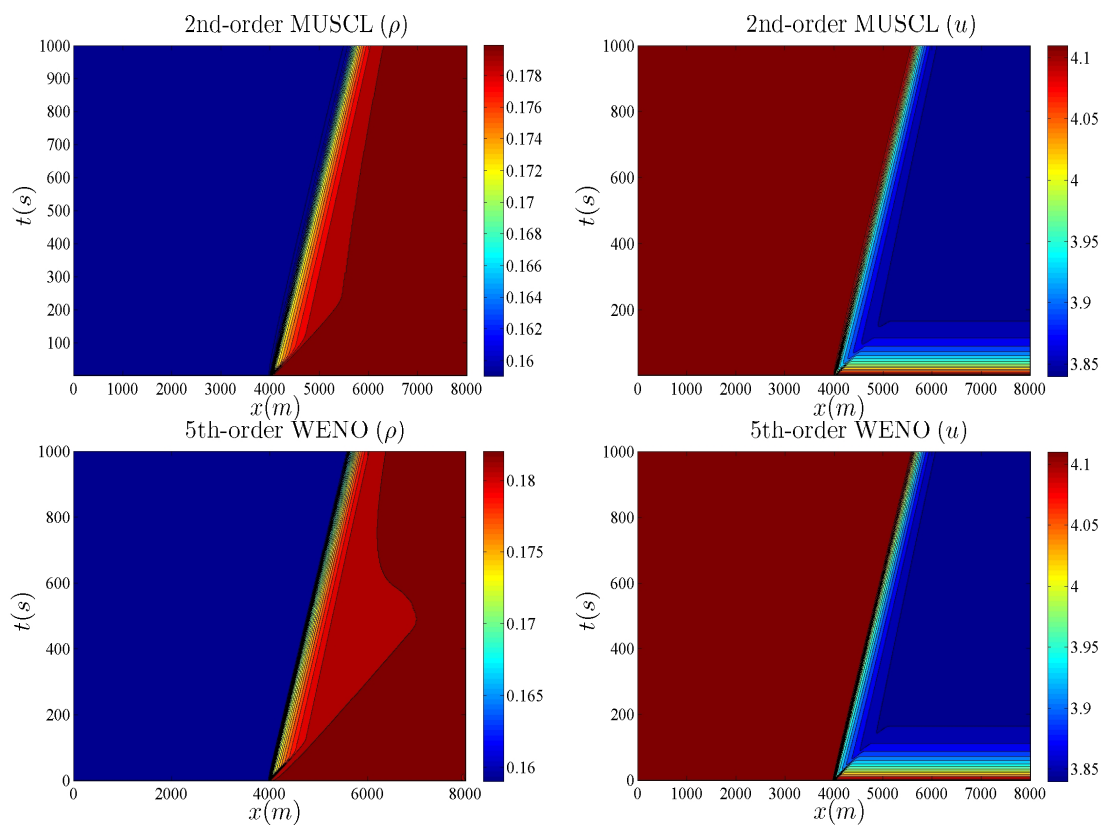


Figure 14: PW model: Formation of shock waves for RP4

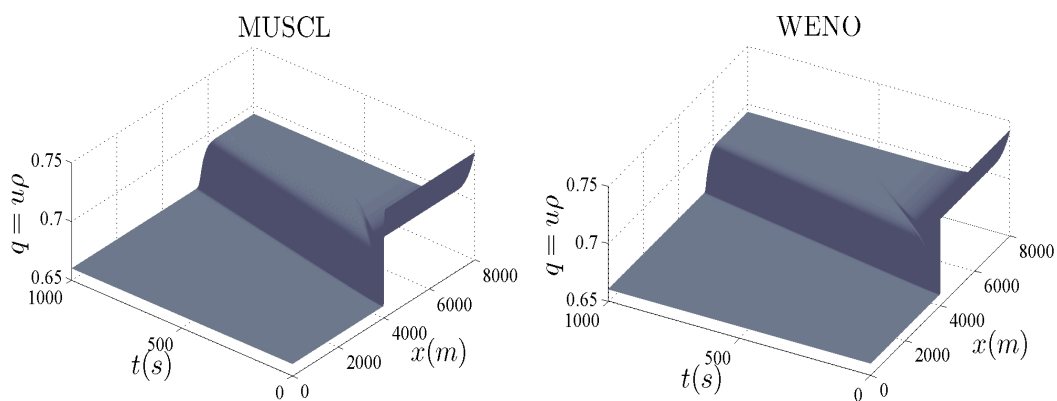


Figure 15: PW model: Formation of a shock wave for RP4, solutions' evolution for q

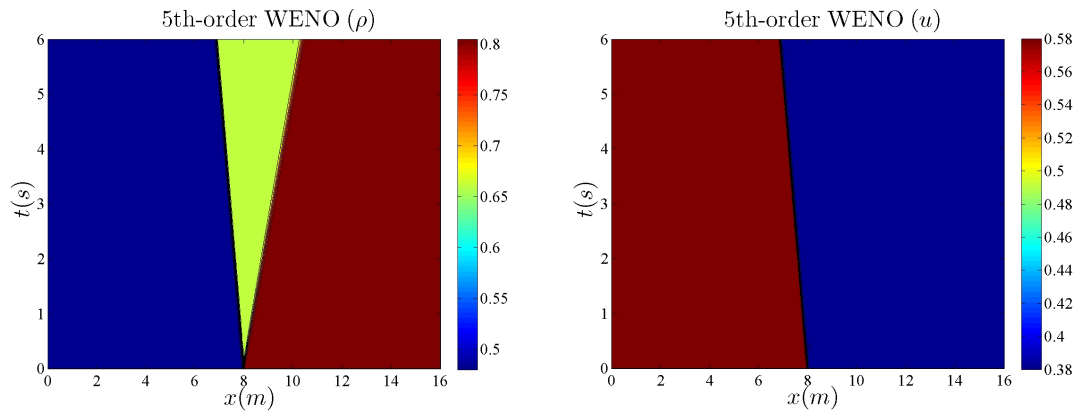


Figure 16: AR model: $S_1 - C_2$ wave solutions for at $t = 6s$

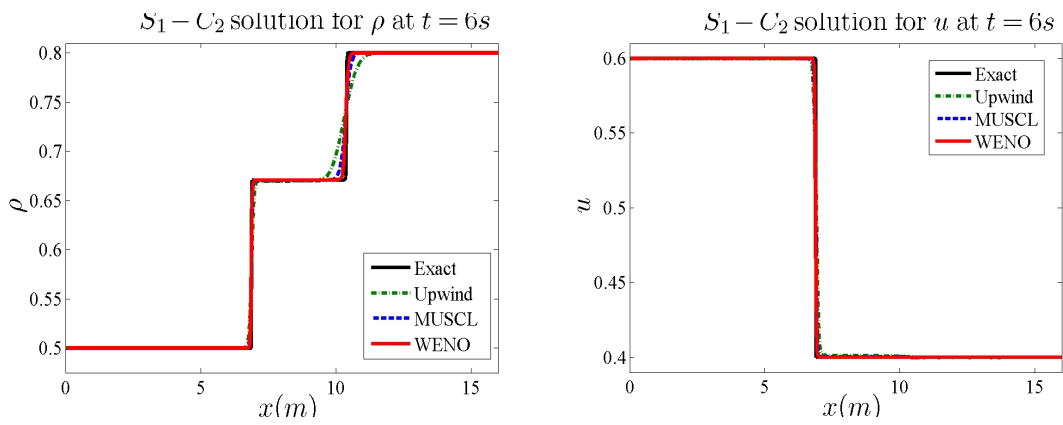


Figure 17: AR model: $S_1 - C_2$ wave solutions comparison at $t = 6s$

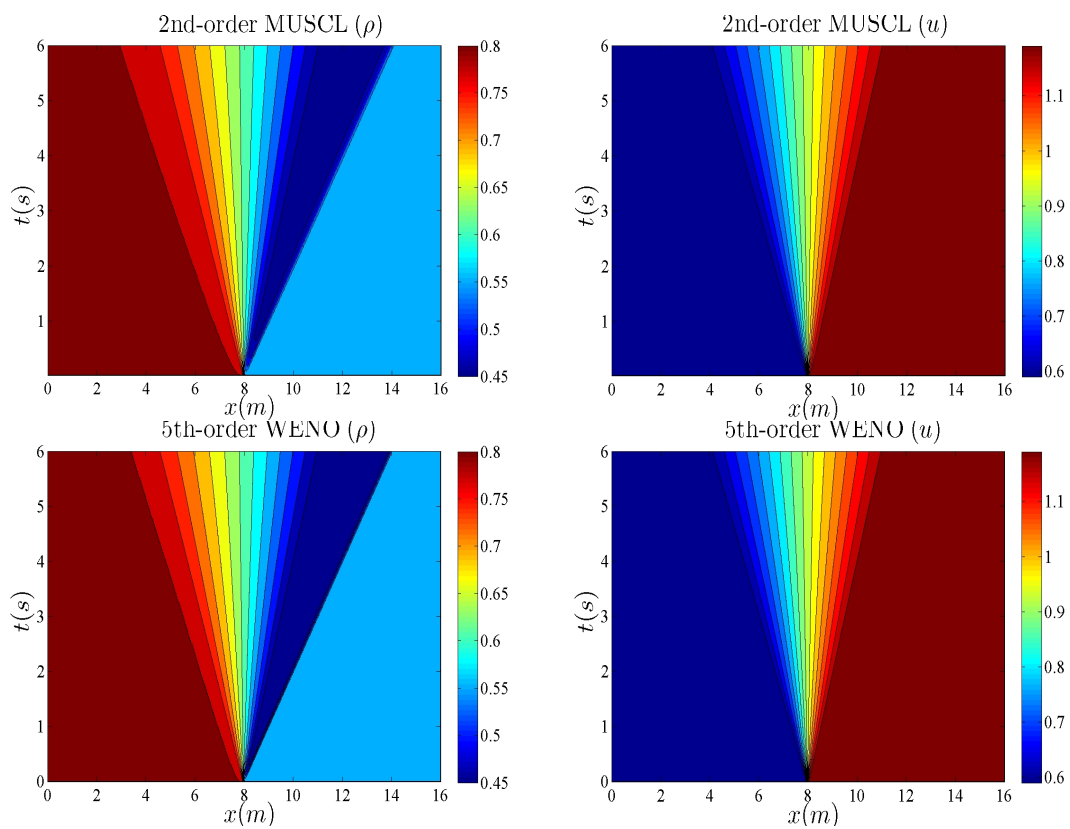


Figure 18: AR model: $R_1 - C_2$ solutions

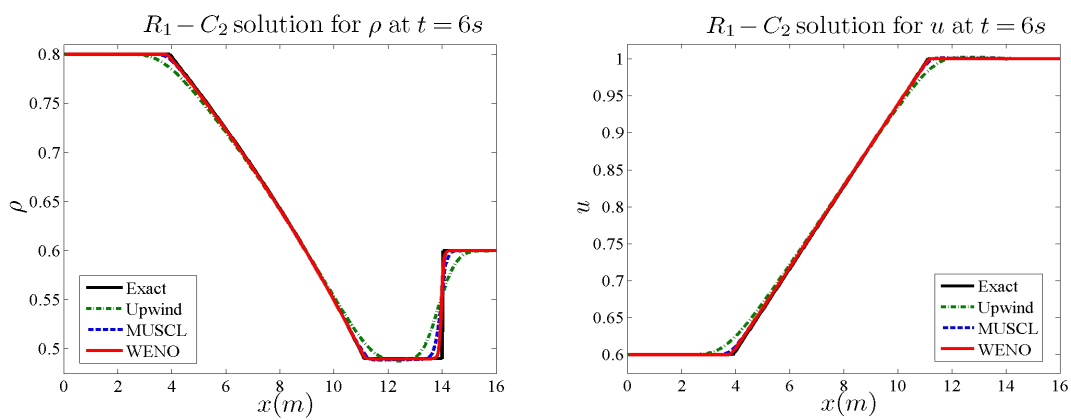


Figure 19: AR model: $R_1 - C_2$ wave solutions comparison at $t = 6s$

AR: Case 3. The initial condition for this problem is

$$[\rho(x, 0), u(x, 0)] = \begin{cases} [\rho_l, u_l] = [0.5, 0.6], & \text{for } x \leq 8, \\ [\rho_r, u_r] = [0, 1], & \text{for } x > 8 \end{cases} \quad (45)$$

and the exact solution in this case is a single rarefaction wave going to the right. The difficulty in this problem has to do with the computation of the correct transition to the free-flow region. To achieve this, a finer grid of $npts = 1200$ had to be used. In addition, a threshold parameter of value 10^{-6} was introduced for density, below which the flow variables were assumed to be zero. The time evolution of density and velocity for the MUSCL and WENO schemes are presented in Fig. 20 and comparison with the exact solution in Fig. 21. Noticeable differences can be observed in the transition region with the WENO scheme being in close agreement with the exact solution

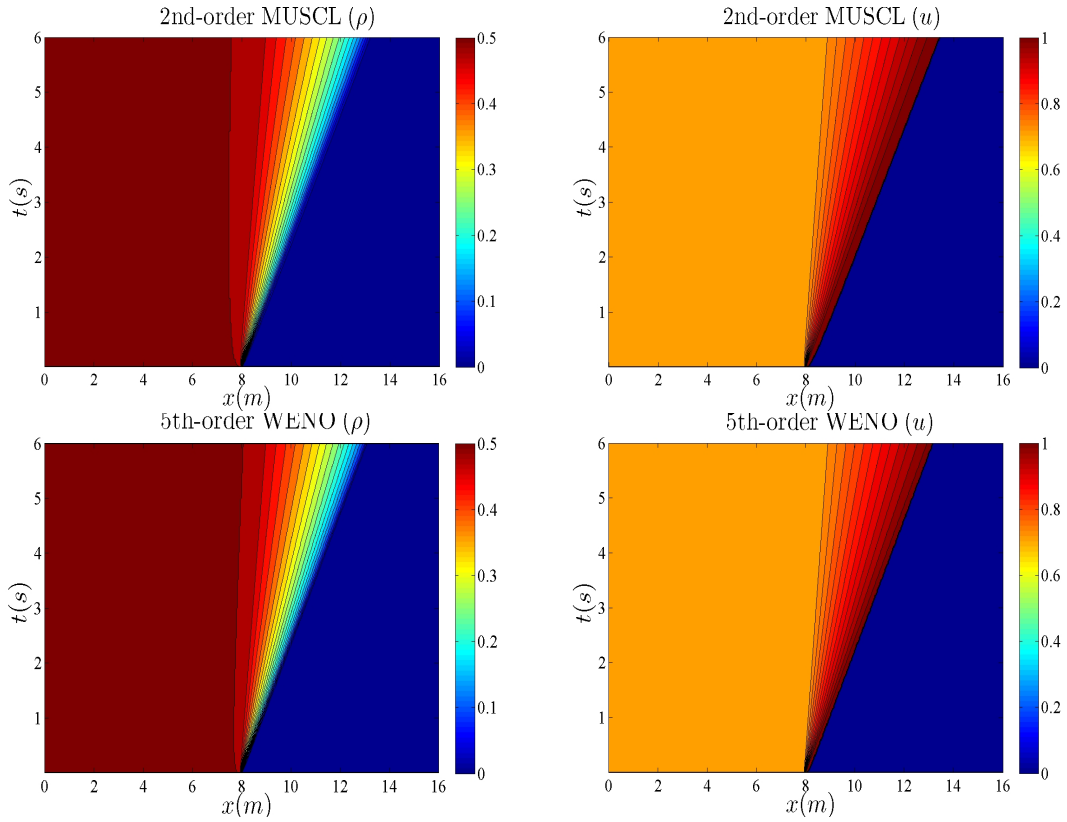


Figure 20: AR model: Rarefaction solution

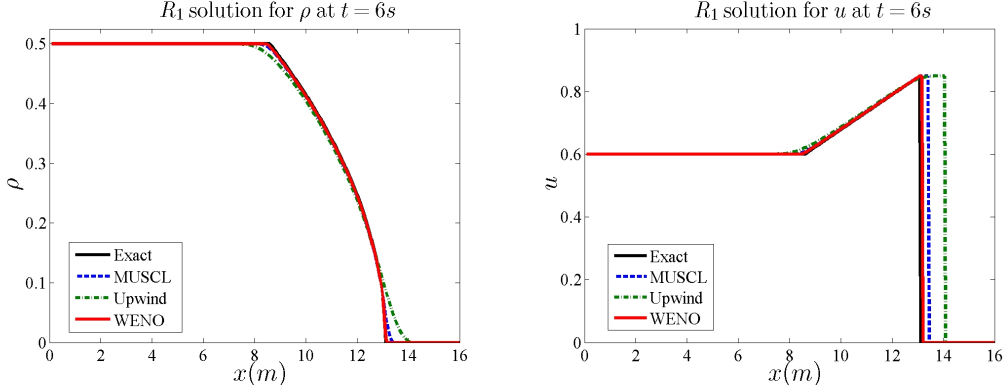


Figure 21: AR model: Rarefaction wave solutions comparison at $t = 6s$

AR: Case 4. For this test case, the situation of faster vehicles downstream followed by slower ones from behind is considered. The initial condition for this problem is

$$[\rho(x, 0), u(x, 0)] = \begin{cases} [\rho_l, u_l] = [0.4, 0.1], & \text{for } x \leq 8, \\ [\rho_r, u_r] = [0.1, 0.9], & \text{for } x > 8. \end{cases} \quad (46)$$

The exact solution of this problem is now given by a rarefaction wave connected to a vacuum state, which is followed by a contact discontinuity going downstream. This is a demanding test case due to the appearance of the vacuum and it is a challenge for any numerical scheme to correctly resolve the transition wave that connects the rarefaction wave to the vacuum state. In addition, the velocity is not defined from the conserved variable $\rho(v + P(\rho))$ in (5). However, using again a finer grid and the tolerance parameter as in the previous test case, a stable numerical solution can be obtained for all scheme as shown in Fig. 22. Important observations can be made from the results. First it is evident that the upwind scheme cannot predict the vacuum state, as can be clearly seen from the velocity evolution, while the higher-order schemes can. Furthermore, the WENO scheme almost perfectly predicts the appearance of the vacuum and the transition wave that connects the rarefaction with the vacuum state. This can be also verified in the comparison with the exact solution in Fig 23. Finally, the spatio-temporal evolution of the density and flow rate computed with the WENO scheme is presented in Fig. 24.

Next, the application of the numerical schemes to the ARZ model are presented. For the simulations, we set $\rho_{\max} = 1$ and $u_{\max} = 1$. The computational domain is of length $L = 1$ and is discretized with a grid of $n_{pts} = 200$ points.

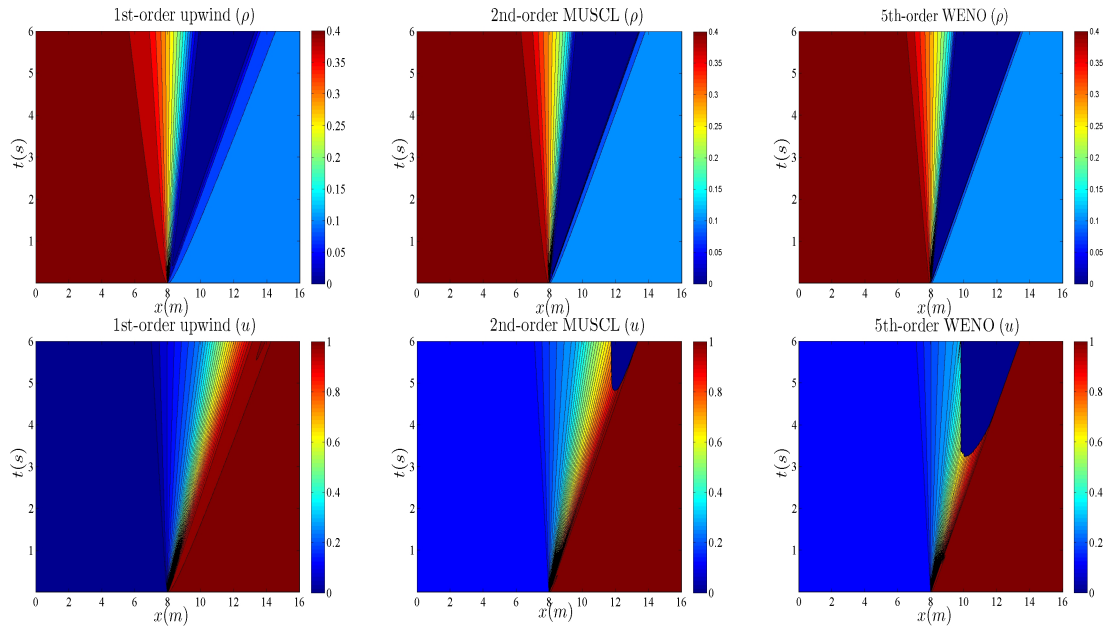


Figure 22: AR model: Vacuum wave solutions for ρ (top) and u

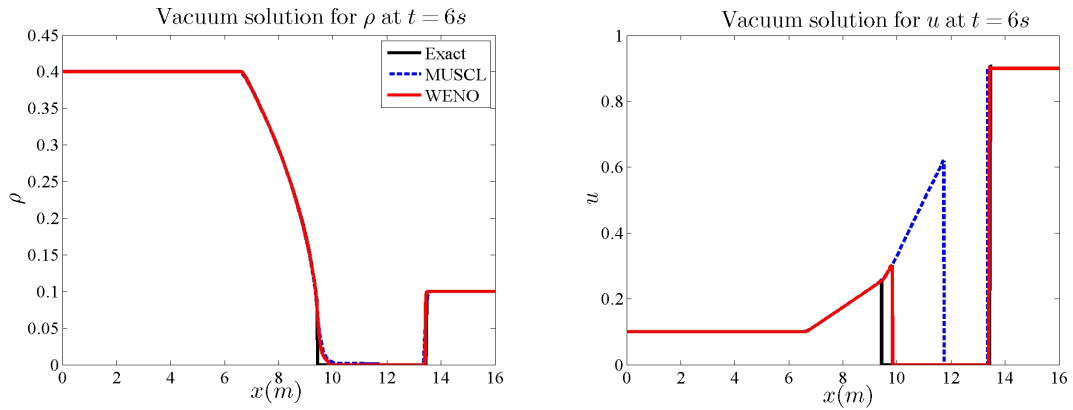


Figure 23: AR model: Vacuum wave solutions comparison at $t = 6s$

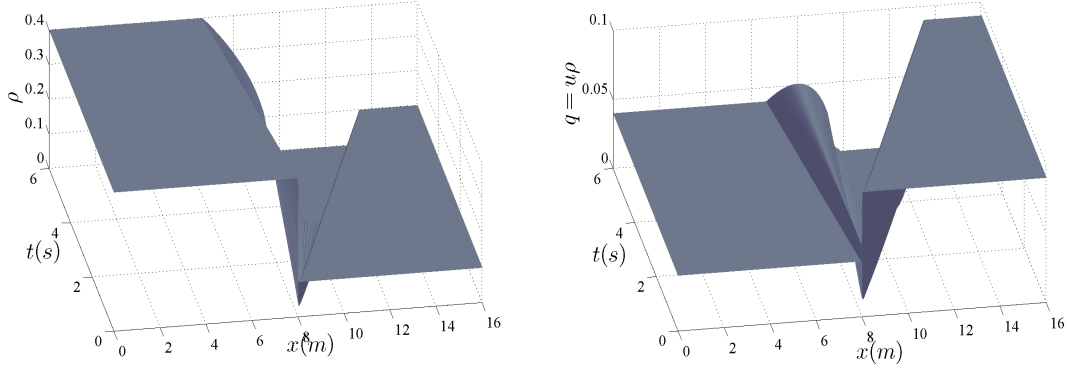


Figure 24: Vacuum solution for the AR model with the WENO relaxation scheme

ARZ: Case 1. The first scenario has the following initial condition

$$[\rho(x, 0), u(x, 0)] = \begin{cases} [\rho_l, u_l] = [0.5, 0.7], & \text{for } x \leq 0.5, \\ [\rho_r, u_r] = [0.5, 0.1], & \text{for } x > 0.5, \end{cases} \quad (47)$$

which satisfies the condition $u_r \leq u_l + V^e(\rho)$ and according to [42] produces a solution consisting of a shock wave followed by a contact discontinuity. The final time is $T_f = 0.8s$ in this case. The spatio-temporal evolution for the density for the high-resolution relaxation schemes is shown in Fig. 25. The sharper resolution of the numerical solution for the WENO scheme, especially for the contact discontinuity is evident. Further, in Fig. 26, a comparison of the solutions for the two schemes for all important variables is presented. The results confirm the sharper representation of the solution by the WENO scheme. As for the previous traffic model, the solutions are stable and non-oscillatory for both schemes.

ARZ: Case 2. The second scenario has the following initial condition

$$[\rho(x, 0), u(x, 0)] = \begin{cases} [\rho_l, u_l] = [0.2, 0.5], & \text{for } x \leq 0.5, \\ [\rho_r, u_r] = [0.9, 0.1], & \text{for } x > 0.5, \end{cases} \quad (48)$$

which now satisfy the condition $\chi = \rho(u - V^e(\rho)) < 0$ and according to [42] produces again a solution consisting of a shock wave followed by a contact discontinuity. The spatio-temporal evolution for the density for the high-resolution relaxation schemes is shown in Fig. 27, while comparisons for density and the conserved variable χ are shown in Fig. 28. Both schemes retain the negative values of the relative flow, and, similar to the previous case, the results confirm the sharper representation of the solution by the WENO scheme.

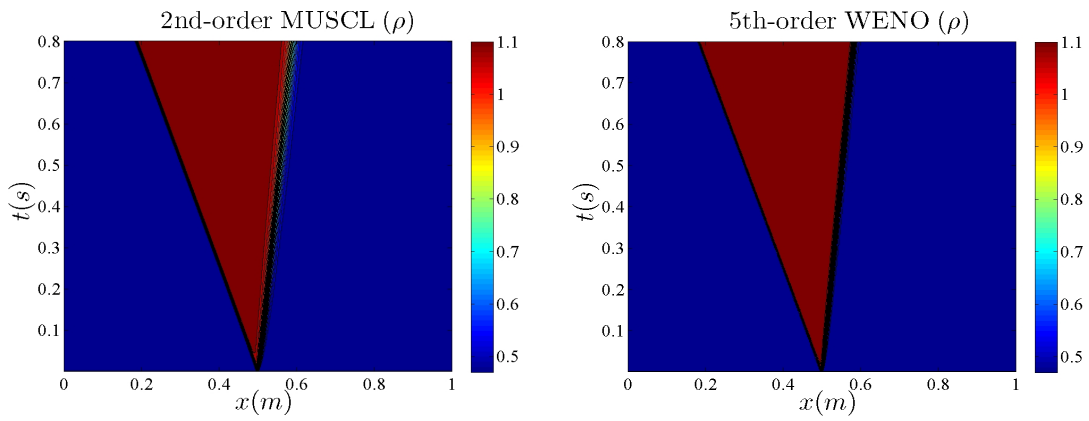


Figure 25: ARZ model: $S_1 - C_2$ solutions' evolution

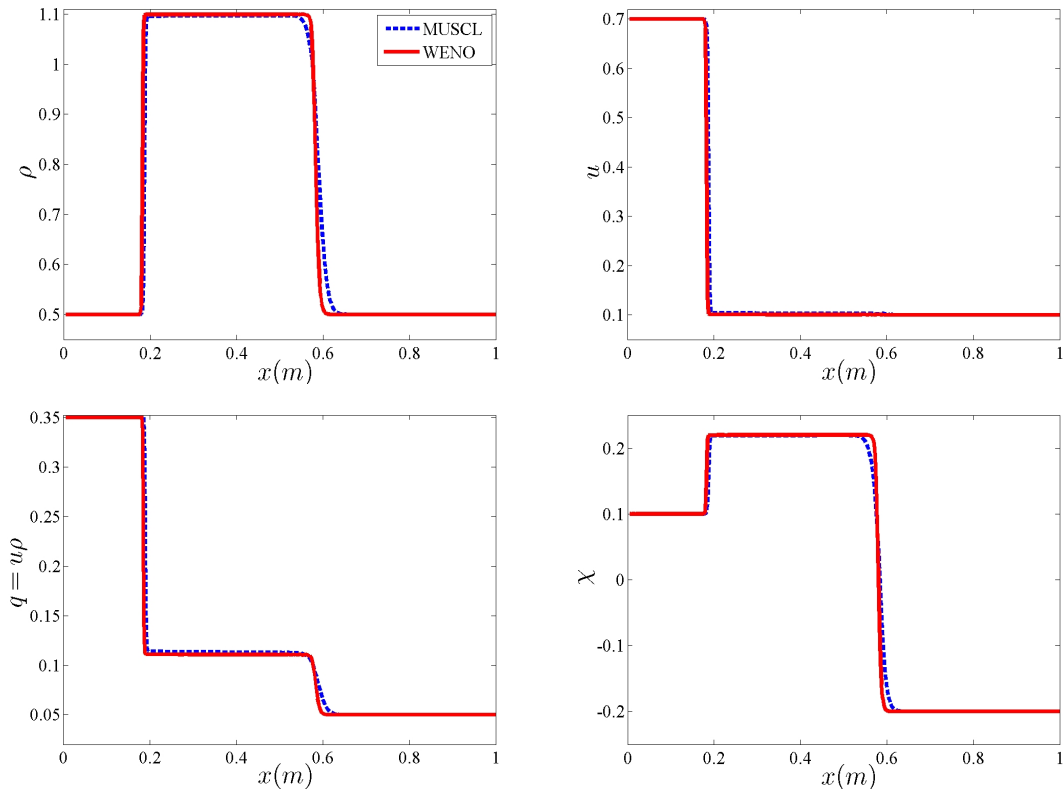


Figure 26: ARZ model: $S_1 - C_2$ solutions at $t = 0.8s$

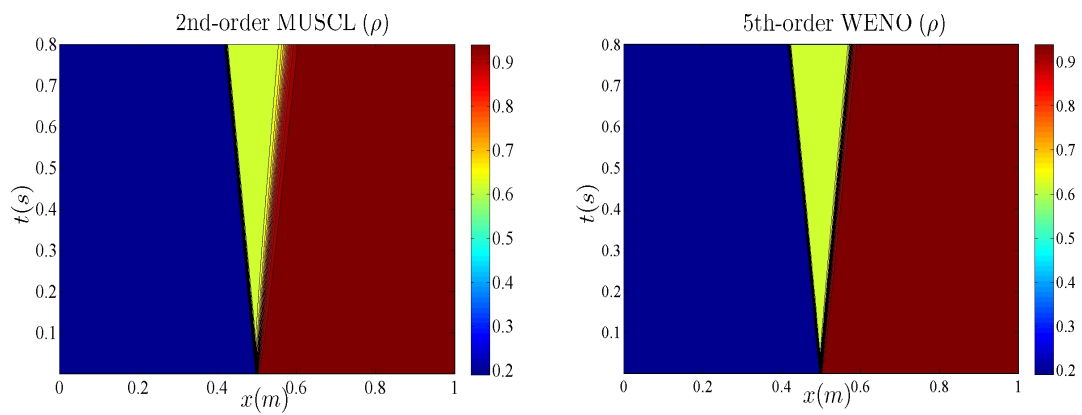


Figure 27: ARZ model: $S_1 - C_2$ solution at $t = 0.8s$

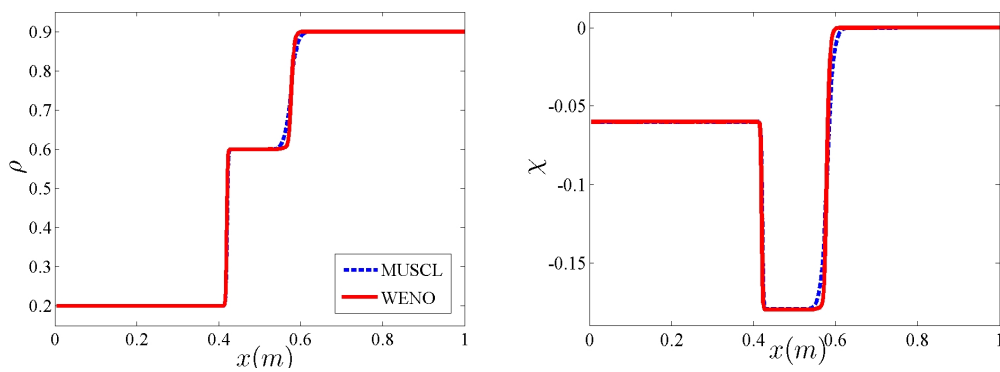


Figure 28: ARZ model: $S_1 - C_2$ solution at $t = 0.8s$

ARZ: Case 3. The final scenario for the ARZ model has the following initial condition

$$[\rho(x, 0), u(x, 0)] = \begin{cases} [\rho_l, u_l] = [0.2, 0.1], & \text{for } x \leq 0.5, \\ [\rho_r, u_r] = [0.5, 0.7], & \text{for } x > 0.5 \end{cases} \quad (49)$$

and is similar to Case 4 for the AR model. The data in this case satisfies the condition $u_r - u_l + V^e(\rho) > u_{max}$. According to [42] the data produces a solution consisting of a rarefaction wave (R_1) followed by another rarefaction (R_2 -fake vacuum wave) and then by a contact discontinuity. Similarly to the AR model Case 4, the difficulty in this problem has to do with the computation of the correct transition to the free-flow region. To this end, a finer grid of $npts = 1000$ had to be used along with the threshold parameter of value for density, below which the flow variables were assumed to be zero. The time evolution of the velocity for the MUSCL and WENO schemes is presented in Fig. 29 where the appearance of the vacuum state is evident for both schemes. Actually, as it can be seen in Fig. 30, both schemes predict very similarly the transition region which can also be clearly seen in Fig. 31, where the results for the density and flow rate produced by the WENO scheme are presented. The solutions are stable and non-oscillatory for this demanding numerical problem.

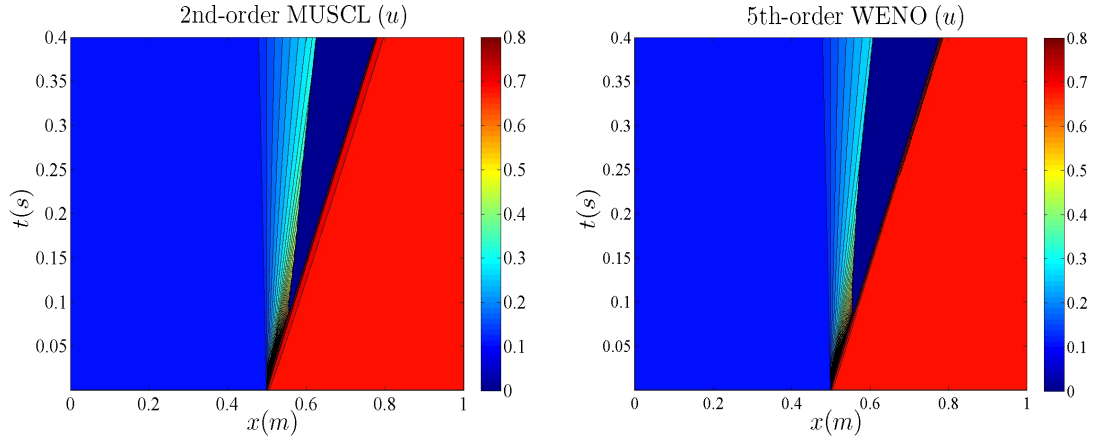


Figure 29: ARZ model: Vacuum wave solutions for u

5.3. Numerical tests for the GKT traffic model

In this section, numerical tests and results are presented for the GKT model detailed in Section 2.3. In all tests and results we concentrate on the application and performance of WENO relaxation scheme due to its enhanced resolution as confirmed in the previous sections. Our aim here is to compute not only basic elementary wave solutions but to expand to more realistic and complex scenarios and to reproduce results from the literature that were obtained with different numerical

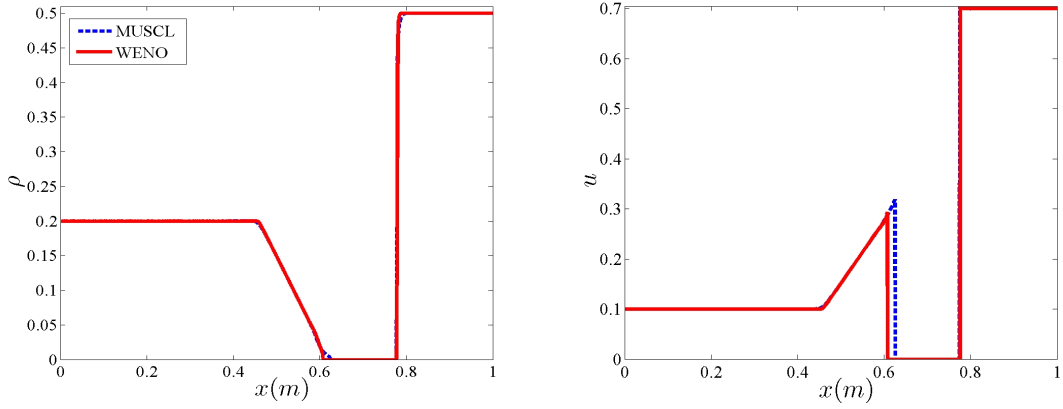


Figure 30: ARZ model: Vacuum solutions at $t = 0.4s$

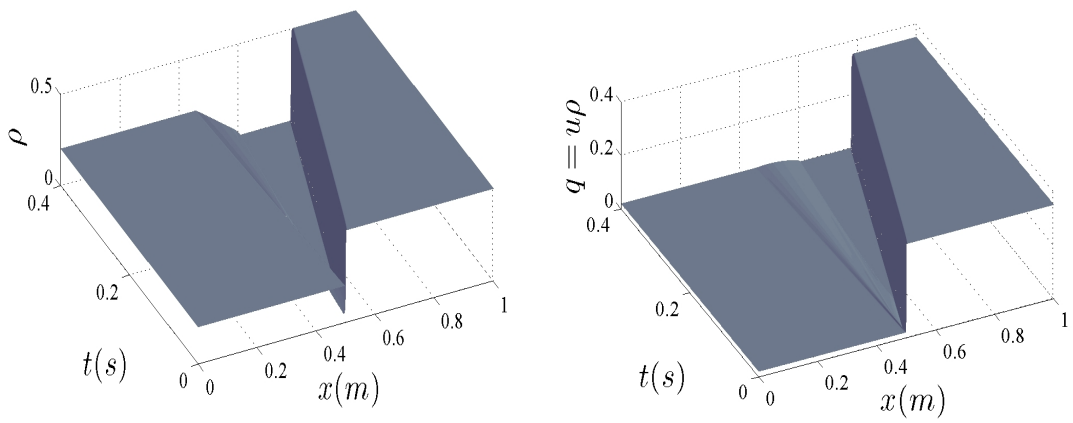


Figure 31: Vacuum solution for the ARZ model with the WENO relaxation scheme

methods. Unless otherwise stated, the model parameters used are those given in Table 1. One of the advantages of the GKT model is that coarser discretizations are possible than in most other traffic models, allowing real-time simulations of larger systems e.g. freeways stretches up to several thousand kilometers.

5.3.1. Traffic flow transitions

The test cases presented first are from [24] and the value of $\Delta A = 0.01$ was used. The first test is for transitions between free traffic at two different vehicle densities in a road with $L = 6000m$ and initial data given as

$$[\rho(x, 0), u(x, 0)] = \begin{cases} [5veh/km, 0km/h], & \text{for } x \leq 0.5km, \\ [15veh/km, 0km/h], & \text{for } 0.5km < x < 3.5km, \\ [5veh/km, 0km/h], & \text{for } x > 3.5km. \end{cases} \quad (50)$$

The numerical results for the upwind and WENO relaxations scheme using $npts = 300$ grid points are shown in Fig. 32 for two time instances. The excessive numerical diffusion and the subsequent smoothening of the traffic fronts for the upwind scheme is once again evident. For the WENO results no numerical dispersion errors, which are usually associated with a slower propagation of waves with small amplitudes and can lead to oscillations in the density behind large gradients [24], can be observed.

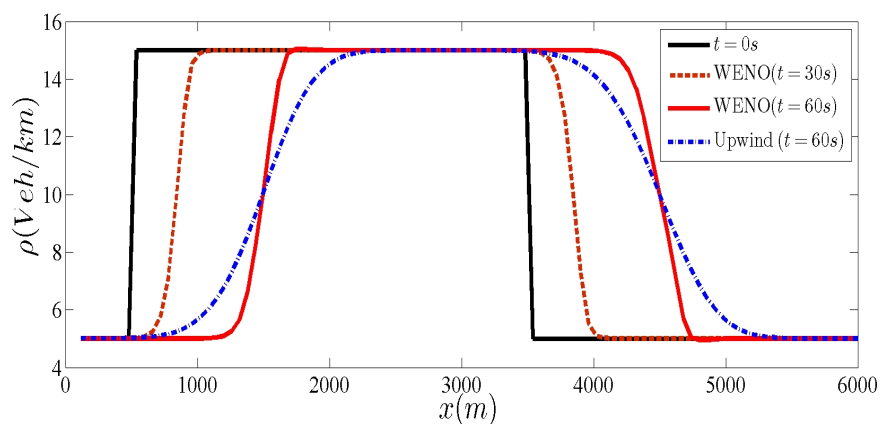


Figure 32: GKT model: Transitions between free traffic at two different vehicle densities

The next case is again from [24] and is for transitions to and from congested traffic with backwards propagating fronts at two different vehicle densities in a road with $L = 6000m$. The initial

data is given as

$$[\rho(x, 0), u(x, 0)] = \begin{cases} [15\text{veh}/\text{km}, 0\text{km}/\text{h}], & \text{for } x \leq 1\text{km}, \\ [125\text{veh}/\text{km}, 0\text{km}/\text{h}], & \text{for } 1\text{km} < x < 3\text{km}, \\ [1\text{veh}/\text{km}, 0\text{km}/\text{h}], & \text{for } x > 3\text{km}. \end{cases} \quad (51)$$

The numerical results for the upwind and WENO relaxation schemes using $npts = 300$ grid points are shown in Fig. 33 for three time instances. Again the WENO results are considered very much accurate. For certain numerical methods nonlinear instabilities may arise at the downstream front of the large amplitude jump or are more sensitive to it [24]. This is of practical importance since (artificial) oscillations or numerical instabilities act like perturbations, which in turn give rise to additional traffic jams that do not correspond to real traffic conditions. Our numerical results were robust in all simulations performed.

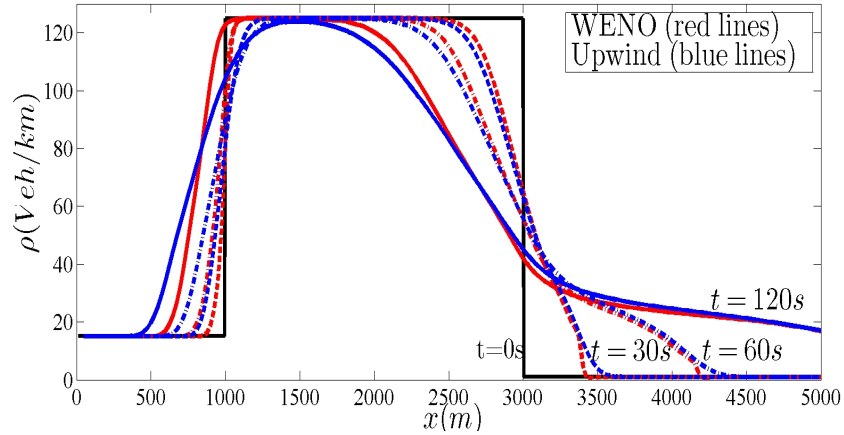


Figure 33: GKT model: Transitions to and from congested traffic with backward propagating front

The next test case is similar to the one presented in [55] and [26] and presents the scenario of propagating fronts emerging between congested and free traffic in a highway of $L = 20\text{km}$ for a total simulation time $T_f = 30\text{min}$. All parameters used in the model are those in Table 1 with the exemption of the acceleration relaxation time set to $\tau = 35\text{s}$. The initial data for this scenario is given by

$$[\rho(x, 0), q(x, 0)] = \begin{cases} [140\text{veh}/\text{km}, 120\text{veh}/\text{h}], & \text{for } x \leq 8.5\text{km}, \\ [1\text{veh}/\text{km}, 120\text{veh}/\text{h}], & \text{for } x > 8.5\text{km}. \end{cases} \quad (52)$$

This scenario, with $\rho_l \gg \rho_r$ in two homogeneous regions, corresponds to a dissolving jam, e.g. after an accident has been cleared, with an outflow to a nearly empty road section. Here, homogeneous Neumann boundary conditions are applied. Fig. 34 shows the spatiotemporal evolution of the

density and flow obtained with the WENO relaxation scheme with $npts = 400$ grid points. The obtained solution evolution describes accurately the expected scenario and the results agree with those presented in [55].

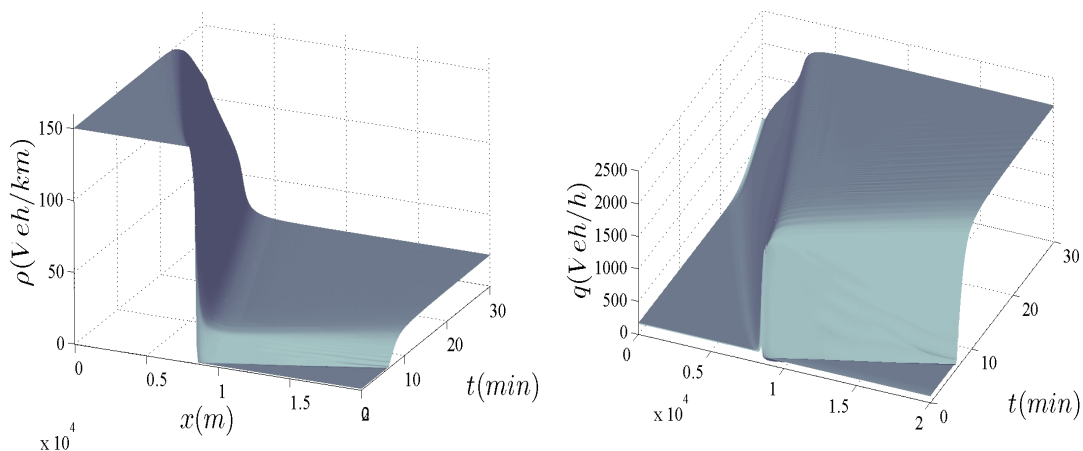


Figure 34: GKT model: Spatiotemporal evolution of downstream-fronts for the density (left) and flow (right)

5.3.2. Homogeneous Traffic with Localized Perturbations

The development of traffic instabilities, starting with almost homogeneous initial traffic, is considered a very strict test of numerical performance. Following [55], we consider a dipole-like initial variation of the average density $\bar{\rho}$ given as

$$\rho(x, 0) = \bar{\rho} + \Delta\rho \left[\cosh^{-2} \left(\frac{x - x_0}{w^+} \right) - \frac{w^+}{w^-} \cosh^{-2} \left(\frac{x - x_0 - \Delta x_0}{w^-} \right) \right]$$

where $w^+ = 201.5$ and $w^- = 805m$ with $\Delta x_0 = w^+ + w^-$. The initial flow $q(x, 0) = q_e(\rho(x, 0)) = \rho V^e$ is assumed in local equilibrium with

$$V^e(\rho) = \frac{\tilde{u}^2}{2u_{\max}} \left(-1 + \sqrt{1 + \frac{4u_{\max}^2}{\tilde{v}}} \right)$$

$$\tilde{u} = \sqrt{\frac{u_{\max}}{\tau\rho A(\rho)P(\rho)}}, \quad P(\rho) = \frac{u_{\max}\rho T^2}{\tau A(\rho_{\max})(1 - \rho/\rho_{\max})^2}.$$

The initial perturbation was set to $\Delta\rho = 10veh/km$ and various tests were performed for different densities $\bar{\rho}$. In the results presented next, we assume traffic flow is in a ring of circumference of

$L = 10km$, thus periodic boundary conditions were implemented, discretized with $npts = 400$ grid points.

In Fig. 35, the results with the WENO relaxation scheme for the case of $\bar{\rho} = 10$ are shown. Here, the initial perturbation dissipates, since the traffic density is sufficiently low; meaning that homogeneous traffic is stable at low densities. When the initial density is increased, the initial perturbation eventually leads to instabilities. This can be intuitively understood since for higher densities a higher percentage of drivers approaching a density peak must brake, thus increasing the density peak. Depending on increased values of $\bar{\rho}$, different situations emerge. In Fig. 36,

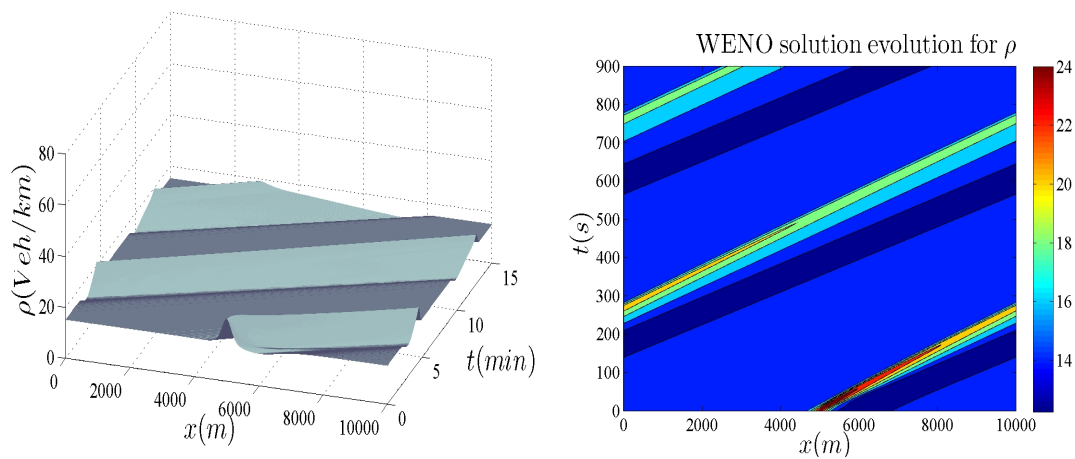


Figure 35: GKT model: Localized Perturbations $\bar{\rho} = 15$, periodic boundary conditions

numerical results obtained with the WENO scheme for $\bar{\rho} = 26$ are shown. In this scenario a single density cluster is formed.

Increasing $\bar{\rho}$ even further to 37, a cascade of traffic jams emerges, i.e. stop-and-go traffic. This is a case which can be difficult to resolve with a low-order scheme. Referring to Fig. 37, the first-order relaxation scheme fails to reproduce all the stop-and-go waves when 400 grid points were used in the numerical simulation. When massively increasing the $npts$ to 4000 (and a grid independent solution has been reached) all emerging waves can be captured by this scheme but, obviously, with a high computational cost. On the other hand, applying the WENO scheme, the correct wave structured is computed only with 400 grid points. This shows the significant advantage that can be gained when one implements a high-resolution scheme in the simulation.

Finally, increasing density $\bar{\rho}$ to 55, a stable regime is reached again. The results for this stable congested flow obtained with the WENO scheme are shown in Fig. 38. We note here that all the results presented in this section are in very good agreement with those presented in [55] and the expected behavior of the GKT model was reproduced by the proposed WENO relaxation scheme.

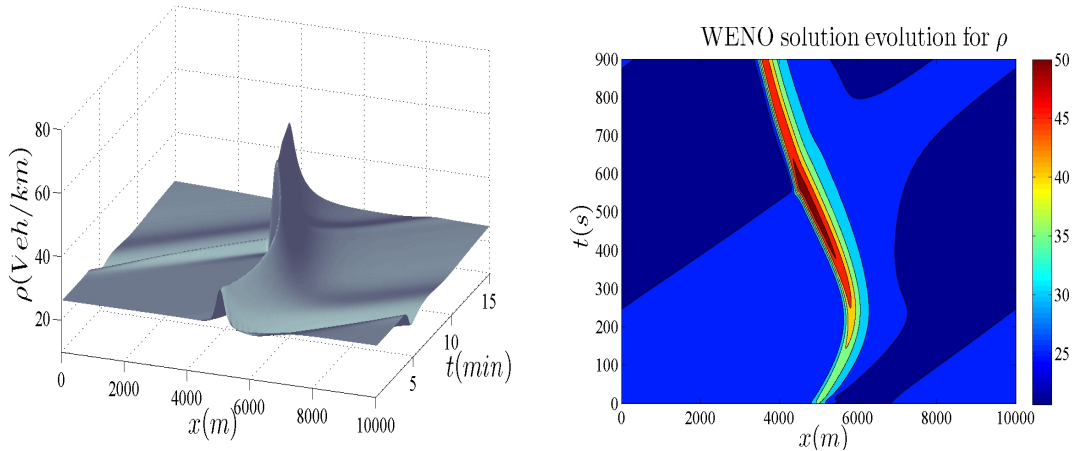


Figure 36: GKT model: Localized Perturbations $\bar{\rho} = 25$, periodic boundary conditions

6. Conclusions

Relaxation schemes have been studied for computing numerical solutions of various, well-known, macroscopic two-equation traffic flow models, formulated in conservation law or balance law forms. The main feature of the proposed approach is its accuracy, simplicity and robustness. Finite volume shock capturing spatial discretizations, that are Riemann solver free, have been used providing accurate resolution. To this end, higher-order schemes of second and fifth-order accuracy have been developed. The higher-order schemes outflanked the first order upwind one, with the WENO fifth-order scheme providing the sharpest resolution and description of fine details of the emerging wave structures in the flow even on coarse grids. The results from the approximation of the realistic Gas-Kinetic-based model are of particular interest. Having simplicity as its main advantage and the attractive feature that neither Riemann solvers nor characteristic decomposition are in need, the relaxation approach can be considered as an alternative for practical applications in macroscopic traffic flow modeling. In particular, it is only necessary to provide the flux and source term functions and an estimate of the characteristic speeds. As relaxation is in a sense a flux approximation, we expect to produce reasonable results for any flux function as long as the system remains hyperbolic. Thus, considering different macroscopic models and real life simulations, the present approach is likely to be applicable then too and can be considered for further studies and development.

Acknowledgments

This research was supported by TRAffic MANagement for the 21st century (TRAMAN21) ERC Advanced Investigator Grand under the European Union's Seventh Framework Programme

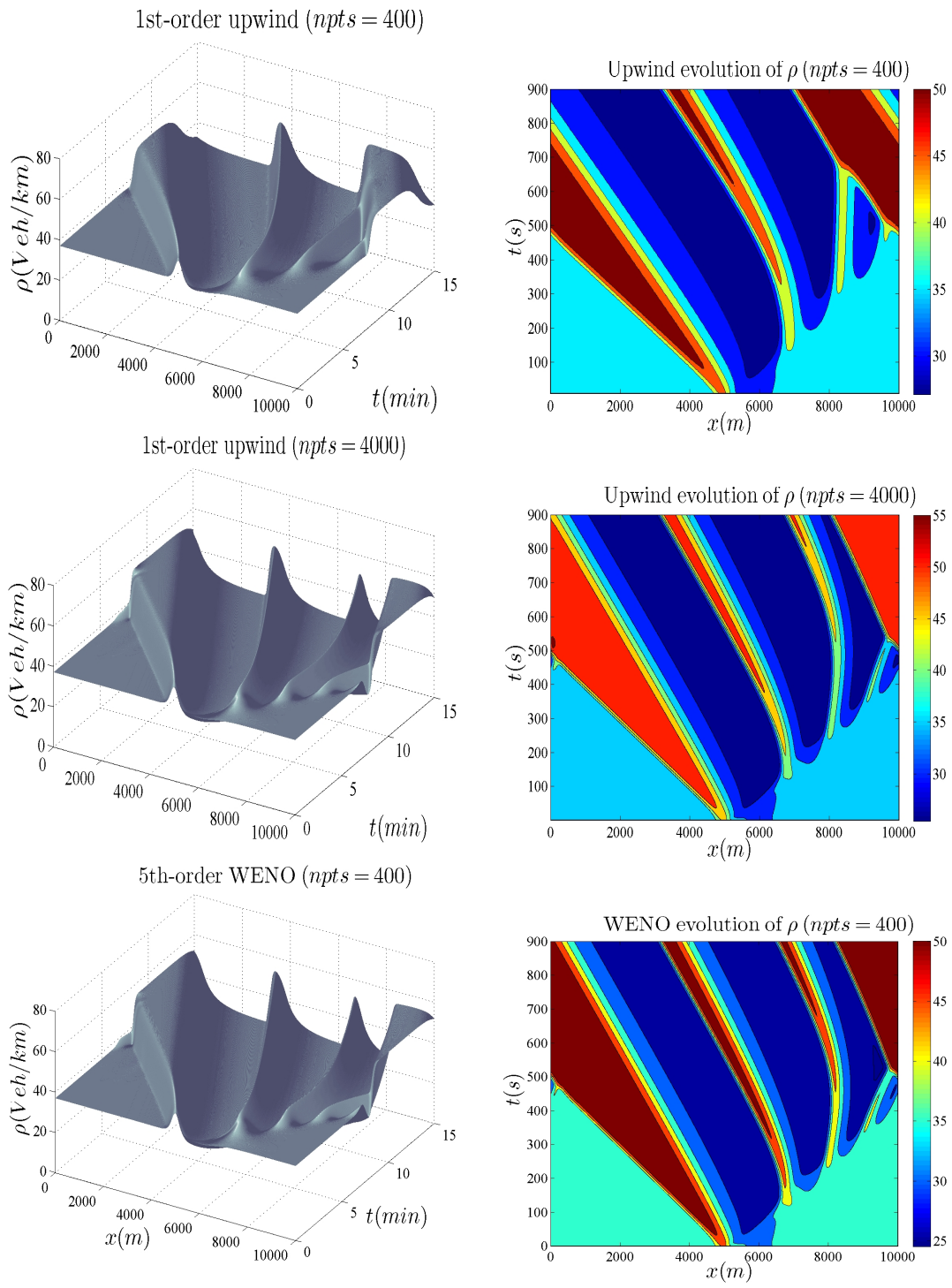


Figure 37: GKT model: Localized Perturbations $\bar{\rho} = 37$, periodic boundary conditions

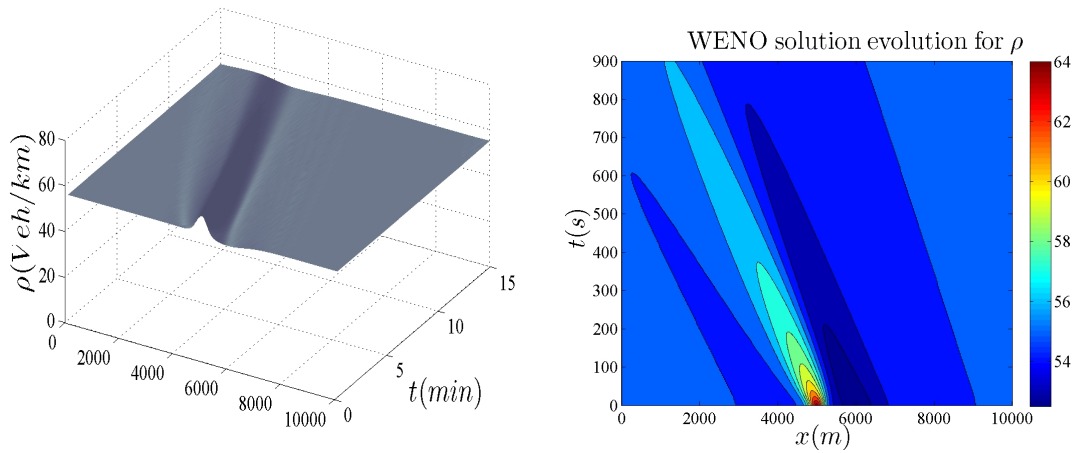


Figure 38: GKT model: Localized Perturbations $\bar{\rho} = 55$, periodic boundary conditions

(FP/2007-20013)

References

- [1] Ankamah J.D., Relaxation scheme for macroscopic traffic flow models, M.Sc. thesis, Department of Mathematics TU-Kaiserlautern and TU-Eindhoven, 2012.
- [2] Aw A. and Rascle M., Resurrection of second-order models of traffic flow, *SIAM J. App. Math.*, **60**, 916-938, 2000.
- [3] Ascher U., Ruuth S. and Spiteri R., Implicit-explicit Runge-Kutta methods for time-dependent partial differential equations, *Appl. Numer. Math.*, **25**:151-167, 1997.
- [4] Banda M. K., Variants of relaxed schemes and two-dimensional gas dynamics, *J. Comput. Appl. Math.* **175**: 41-62, 2005.
- [5] Banda M. K., Non-oscillatory relaxation schemes for one-dimensional ideal magnetohydrodynamic equations, *Nonlinear Analysis:Real World Applications*, **10**:3345-3352, 2009.
- [6] Banda M. K. and Seaid M., Higher-Order Relaxation Schemes for Hyperbolic Systems of Conservation Laws, *J. Numer. Math.* **13**:171-196, 2005.
- [7] Bellomo N. and Dogbe C., On the modeling of traffic and crowds: a survey of models, speculations, and perspectives, *SIAM Rev.*, **53**:409-463, 2011.

- [8] Borges R., Carmona M., Costa B. and Don W.-S., An improved weighted essentially non-oscillatory scheme for hyperbolic conservation laws, *J. of Comp. Phys.*, **227**:3191-3211, 2008.
- [9] Burger R., Garcia A., Karlsen K.H., Towers J.T., A family of numerical schemes for kinematic flows with discontinuous flux, *J. Eng. Math.*, **60**, 387-425, 2008.
- [10] Coclite G.M., Garavello M. and Piccoli B., Traffic flow on a road network, *SIAM J. Math. Anal.*, **36**:1861-1886, 2005.
- [11] Chalabi A., Convergence of relaxation schemes for hyperbolic conservation laws with stiff source terms. *Math. Comput.*, **68**:955-970, 1999.
- [12] Chalabi A. and Seghir D., Convergence of relaxation schemes for initial boundary value problems for conservation laws, *Comput. Math. Appl.* **43** (8-9):1079-1093, 2002.
- [13] Chen J.-Z. and Shi Z-K., Application of a fourth-order relaxation scheme to hyperbolic systems of conservation laws, *Acta Mech. Sinica*, 22(1):84-92, 2006.
- [14] Chen J.-Z., Shi Z-K., and Hu Y-M., A relaxation scheme for a multi-class Lighthill-Withan-Richards traffic model, *J. Zhejiang Univ Sci A*, **10**:1835-1844, 2009.
- [15] Chen J.-Z., Shi Z-K., and Hu Y-M., Numerical solutions of a multiclass traffic flow model on an inhomogeneous highway using a high-resolution relaxed scheme, *J. Zhejiang Univ Sci C (Comput & Electron)*, **13**:29-36, 2012.
- [16] Daganzo C., Requiem for second-order fluid approximations to traffic flow, *Transportation Res. B*, **25**:277-286, 1995.
- [17] Del Castillo J., Pintado, P. and Benitez F., The reaction of drivers and the stability of traffic flow, *Transportation Res. B*, **28**, 35-60, 1994.
- [18] Delis A. I. and Katsaounis Th., Relaxation schemes for the shallow water equations, *Int. J. Numer. Meth. Fluids*, **41**: 695-719, 2003.
- [19] Delis A. I. and Katsaounis Th., A generalized relaxation method for transport and diffusion of pollutant models in shallow water, *Comp. Meth. Appl. Math.*, **4**(4):410-430, 2004.
- [20] Delis A. I. and Katsaounis Th., Numerical solution of the two-dimensional shallow water equations by the application of relaxation methods. *Appl. Math. Model.*, **29**:754-783, 2005.
- [21] Delis A. I., Papoglou P., Relaxation approximation to bed-load sediment transport, *J. of computational and Applied Mathematics*, **213**:521-546, 2008.
- [22] Evje S. and Fjelde K. K., Relaxation schemes for the calculation of two-phase flow in pipes, *Mathematical and Computer Modelling* **36**(4-5):535-567, 2002.

- [23] Garavello M. and Goatin P., The Aw-Rascle traffic model with locally constrained flow, *J. Of Mathematical Analysis and Applications*, **378**:634-648, 2011.
- [24] Helbing D. and Treiber M., Numerical simulation of macroscopic traffic equations, *Computing in Science and Engineering*, **1**(5):89-99, 1999.
- [25] Helbing D., Traffic and related self-driven many-particle systems”, *Reviews of Modern Physics*, **73**:1067-1141, 2001.
- [26] Helbing D., Hennecke A., Shvetsov V. and Treiber, M., MASTER: Macroscopic traffic simulation based on a gas-kinetic, non-local traffic model, *Transportation Research Part B: Methodological*, **35**(2):183-211, 2001.
- [27] Helbing D., Hennecke A., Shvetsov, V. and Treiber M., Micro- and macro-simulation of freeway traffic, *Mathematical and Computer Modelling*, **35**:517-547, 2002.
- [28] Helbing D. and Johansson, A.F., On the controversy around Daganzo’s requiem for and Aw-Rascle’s resurrection of second-order traffic flow models, *The European Physical Journal B*, **69**, 549-562, 2009.
- [29] Hermann M. and Kerner B.S. Local cluster effects in different traffic flow models *Physica A*, **255**:163-198, 1998.
- [30] Herty M., Pareschi, L. and Seaid, M., Discrete-velocity models and relaxation schemes for traffic flows, *SIAM J. Sci. Comput*, **28**:1582-1596, 2006
- [31] Hoogendoorn, S.P., Bovy, P.H.L., State-of-the-art of vehicular traffic flow modelling, Proceedings of the Institution of Mechanical Engineering. Part I: Journal of Systems and Control Engineering, **215**:283-303, 2001.
- [32] Jiang G.S., Shu C.-W., Efficient implementation of weighted ENO schemes, *Journal of Computational Physics*, **126**:202-228, 1996.
- [33] Kerner B.S. and Konhauser P., Structure and parameters of clusters in traffic flow, *Physical Review E*, **50**, 54-83, 1994.
- [34] Jin S. and Xin Z., The relaxing schemes of conservation laws in arbitrary space dimensions, *Comm. Pure Appl. Math.*, **48**:235-277, 1995.
- [35] Jin W.L. and Zhang H.M., Solving the Payne-Whitham traffic flow model as a hyperbolic system of conservation laws with relaxation, Technical Report, University of California, Davis, 2001.
- [36] LeVeque R.J. and Pelanti M., A class of Approximate Riemann solvers and their relation to relaxation schemes, *J. Comp. Phys.*, **172**:572-592, 2001.

- [37] LeVeque R. J., *Finite Volume Methods for Hyperbolic Problems*. Cambridge University Press, 2002.
- [38] Li X. G., Yu X.J. and Chen G. N., The third-order relaxation schemes for hyperbolic conservation laws, *J. Comput. Appl. Math.*, **138**(1):93-108, 2002,
- [39] Lighthill M.J. and Witham G.B., On kinematic waves I: Flood movement in long rivers, On kinematic waves II: A theory of traffic flow on long crowded roads, *In Proceedings of the Royal Society of London series A, Mathematical and Physical Sciences*, **229**:281-345, 1955.
- [40] Liu T.P., Hyperbolic conservation laws with relaxation, *Comm. Math. Phys.*, **108**:153-175, 1987.
- [41] Liu G., Lyrintzis A.S. and Michalopoulos P.G., Improved high-order model for freeway traffic flow, *Transportation Research Record*. 1644:37-47, 1998.
- [42] Mhammer S., Lebacque J.P. and Salem H.H., Riemann Problem resolution and Godunov scheme for the Aw-Rascle-Zhang model, *Trans. Sci.* **43**:531-545, 2009.
- [43] Natalini R. Convergence to equilibrium for the relaxation approximations of conservation laws. *Comm. Pure Appl. Math.*, **49**:795–823, 1996.
- [44] Ngoduy D., Hoogendorn S.P., and Van Zuylen H.J., Comparison of numerical schemes for macroscopic traffic flow models, *Transportation Research Record: Journal of the Transportation Research Board*, No. 1876, 52-61, 2004.
- [45] Ngoduy D., Instability of cooperative adaptive cruise control traffic flow: A macroscopic approach, *Commun Nonlinear Sci Numer Simulat.*, **18**:2838-2851, 2013.
- [46] Papageorgiou, M., Some remarks on macroscopic traffic flow modelling, *Transportation Research Part B*, **32**, 323-329, 1998.
- [47] Payne H.J., Models of freeway traffic and control, in *Mathematical Models of Public Systems*, Vol. 1 of Simulation Councils Proc. Ser., 51-60, 1971.
- [48] Pareschi L. and Russo G., Implicit-explicit Runge-Kutta schemes and applications to hyperbolic systems with relaxation *J. Sci. Comput.*, **25**(1):129-155, 2005.
- [49] Richards P.I., Shock waves on the highway, *Operations Research, The Journal of the Operations Research Society of America*, **4**:42-51, 1956.
- [50] Seaid M., Non-oscillatory relaxation methods for the shallow water equations in one and two space dimensions, *Int. J. Num. Meth. Fluids*, **46**:457-484, 2004.
- [51] Seaid M., High-Resolution Relaxation Scheme for the Two-Dimensional Riemann Problems in Gas Dynamics, *Numer. Methods for Partial Differential Equations*, **22**:397-413, 2006.

- [52] Seaid M., Improved Applications of Relaxation Schemes for Hyperbolic Systems of Conservation Laws and Convection-Diffusion Problems, *Comp. Meth. Appl. Math.* **6**(2):56-86, 2006.
- [53] Seaid M., Stable numerical methods for conservation laws with discontinuous flux function, *Applied Mathematics and Computation*, **175**:383-400, 2006.
- [54] Sweby P. K., High Resolution Schemes Using Flux Limiters for Hyperbolic Conservation Laws, *SIAM J. Numer. Anal.*, **21**:995, 1984.
- [55] Treiber M., Hennecke A. and Helbing D., Derivation, properties, and simulation of a gas-kinetic-based, nonlocal traffic model, *Physical Review E - Statistical Physics, Plasmas, Fluids, and Related Interdisciplinary Topics*, **59**(1):239-253, 1999.
- [56] Treiber M. and Kesting A. Traffic flow dynamics: data, models and simulation, Springer, 2013.
- [57] Wiens J.K., Stockie, J.M. and Williams, J.F., Riemann solver for a kinetic wave traffic model with discontinuous Flux, *J. of Computational Physics*, **242**:1-23, 2013
- [58] Witham G.B., Linear and nonlinear waves, John Wiley and Sons, New York, 1974
- [59] Wong G.C.K. and Wong S.C., A multi-class traffic flow model - an extension of LWR model with heterogeneous drivers", *Transportation Research Part A*, **36**:827-841, 2002.
- [60] Zhang H.M., A non-equilibrium traffic model devoid of gas-like behavior, *Transportation Research B*, **36**:275-290, 2002.
- [61] Zhang H.M., Kuhne R and Michalopoulos P., Continuum Flow Models, Chapter 3 in Monograph on Traffic flow Theory, 2003.
- [62] Zhang M., Shu C.-W., Wong, G.C.K. and Wong, S.C., A weighted essentially non-oscillatory numerical scheme for a multi-class Lighthill-Whitham-Richards traffic flow model, *Journal of Computational Physics*, **191**:639-659, 2003.
- [63] Zhang H.M., Anisotropic property revisited-does it hold in multi lane traffic?, *Transportation Research Part A*, **37**, 561-577, 2003.
- [64] Zhang P., Wong S.C. and Shu, C.-W., A weighted essentially non-oscillatory numerical scheme for a multi-class traffic flow model on an inhomogeneous highway, *Journal of Computational Physics*, **212**:739-756, 2006.
- [65] Zhang P., Wong S.C. and Dai, S.-Q., A note on the weighted essentially non-oscillatory numerical scheme for a multi-class Lighthill-Whitham-Richards traffic flow model, *Communications in Numerical Methods in Engineering*, **25**:1120-1126, 2009.